Smart and Resilient Infrastructure based on AI and Digital Twin

Lead Guest Editor: Jianyong Shi
Guest Editors: Xin-Zheng Lu, Jiarui Lin, Xuesong Shen, and Pingbo Tang

Smart and Resilient Infrastructure based on AI and Digital Twin

Smart and Resilient Infrastructure based on AI and Digital Twin

Lead Guest Editor: Jianyong Shi
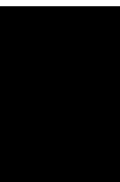Guest Editors: Xin-Zheng Lu, Jiarui Lin, Xuesong Shen, and Pingbo Tang

Zhaofei Chu, China
Wonseok Chung, Republic of Korea
Donato Ciampa, Italy
Gian Paolo Cimellaro, Italy
Francesco Colangelo, Italy
Romulus Costache, Romania
Liviu-Adrian Cotfas, Romania
Antonio Maria D'Altri, Italy
Bruno Dal Lago, Italy
Amos Darko, Hong Kong
Arka Jyoti Das, India
Dario De Domenico, Italy
Gianmarco De Felice, Italy
Stefano De Miranda, Italy
Maria T. De Risi, Italy
Tayfun Dede, Turkey
Sadik O. Degertekin, Turkey
Camelia Delcea, Romania
Cristoforo Demartino, China
Giuseppe Di Filippo, Italy
Luigi Di Sarno, Italy
Fabio Di Trapani, Italy
Aboelkasim Diab, Egypt
Thi My Dung Do, Vietnam
Giulio Dondi, Italy
Jiangfeng Dong, China
Chao Dou, China
Mario D'Aniello, Italy
Jingtao Du, China
Ahmed Elghazouli, United Kingdom
Francesco Fabbrocino, Italy
Flora Faleschini, Italy
Dingqiang Fan, Hong Kong
Xueping Fan, China
Qian Fang, China
Salar Farahmand-Tabar, Iran
Ilenia Farina, Italy
Roberto Fedele, Italy
Guang-Liang Feng, China
Luigi Fenu, Italy
Tiago Ferreira, Portugal
Marco Filippo Ferrotto, Italy
Antonio Formisano, Italy
Guoyang Fu, Australia
Stefano Galassi, Italy

Junfeng Gao, China
Meng Gao, China
Giovanni Garcea, Italy
Enrique García-Macías, Spain
Emilio García-Taengua, United Kingdom
DongDong Ge, USA
Khaled Ghaedi, Malaysia
Khaled Ghaedi, Malaysia
Gian Felice Giaccu, Italy
Agathoklis Giaralis, United Kingdom
Ravindran Gobinath, India
Rodrigo Gonçalves, Portugal
Peilin Gong, China
Belén González-Fonteboa, Spain
Salvatore Grasso, Italy
Fan Gu, USA
Erhan Güneyisi, Turkey
Esra Mete Güneyisi, Turkey
Pingye Guo, China
Ankit Gupta, India
Federico Gusella, Italy
Kemal Hacıefendioğlu, Turkey
Jianyong Han, China
Song Han, China
Asad Hanif, Macau
Hadi Hasanzadehshooiili, Canada
Mostafa Fahmi Hassanein, Egypt
Amir Ahmad Hedayat, Iran
Khandaker Hossain, Canada
Zahid Hossain, USA
Chao Hou, China
Biao Hu, China
Jiang Hu, China
Xiaodong Hu, China
Lei Huang, China
Cun Hui, China
Bon-Gang Hwang, Singapore
Jijo James, India
Abbas Fadhil Jasim, Iraq
Ahad Javanmardi, China
Krishnan Prabhakan Jaya, India
Dong-Sheng Jeng, Australia
Han-Yong Jeon, Republic of Korea
Pengjiao Jia, China
Shaohua Jiang, China

MOUSTAFA KASSEM, Malaysia
Mosbeh Kaloop, Egypt
Shankar Karuppannan, Ethiopia
John Kechagias, Greece
Mohammad Khajehzadeh, Iran
Afzal Husain Khan, Saudi Arabia
Mehran Khan, Hong Kong
Manoj Khandelwal, Australia
Jin Kook Kim, Republic of Korea
Woosuk Kim, Republic of Korea
Vaclav Koci, Czech Republic
Loke Kok Foong, Vietnam
Hailing Kong, China
Leonidas Alexandros Kouris, Greece
Kyriakos Kourousis, Ireland
Moacir Kripka, Brazil
Anupam Kumar, The Netherlands
Emma La Malfa Ribolla, Czech Republic
Ali Lakirouhani, Iran
Angus C. C. Lam, China
Thanh Quang Khai Lam, Vietnam
Luciano Lamberti, Italy
Andreas Lampropoulos, United Kingdom
Raffaele Landolfo, Italy
Massimo Latour, Italy
Bang Yeon Lee, Republic of Korea
Eul-Bum Lee, Republic of Korea
Zhen Lei, Canada
Leonardo Leonetti, Italy
Chun-Qing Li, Australia
Dongsheng Li, China
Gen Li, China
Jiale Li, China
Minghui Li, China
Qingchao Li, China
Shuang Yang Li, China
Sunwei Li, Hong Kong
Yajun Li, China
Shun Liang, China
Francesco Liguori, Italy
Jae-Han Lim, Republic of Korea
Jia-Rui Lin, China
Kun Lin, China
Shibin Lin, China

Tzu-Kang Lin, Taiwan
Yu-Cheng Lin, Taiwan
Hexu Liu, USA
Jian Lin Liu, China
Xiaoli Liu, China
Xuemei Liu, Australia
Zaobao Liu, China
Zhuang-Zhuang Liu, China
Diego Lopez-Garcia, Chile
Cristiano Loss, Canada
Lyan-Ywan Lu, Taiwan
Jin Luo, USA
Yanbin Luo, China
Jianjun Ma, China
Junwei Ma, China
Tian-Shou Ma, China
Zhongguo John Ma, USA
Maria Macchiaroli, Italy
Domenico Magisano, Italy
Reza Mahinroosta , Australia
Yann Malecot, France
Prabhat Kumar Mandal, India
John Mander, USA
Iman Mansouri, Iran
André Dias Martins, Portugal
Domagoj Matesan, Croatia
Jose Matos, Portugal
Vasant Matsagar, India
Claudio Mazzotti, Italy
Ahmed Mebarki, France
Gang Mei, China
Kasim Mermerdas, Turkey
Giovanni Minafò, Italy
Masoomeh Mirrashid, Iran
Abbas Mohajerani, Australia
Fadzli Mohamed Nazri, Malaysia
Fabrizio Mollaioli, Italy
Rosario Montuori, Italy
H. Naderpour, Iran
Hassan Nasir, Pakistan
Hossein Nassiraei, Iran
Satheeskumar Navaratnam, Australia
Ignacio J. Navarro, Spain
Ashish Kumar Nayak, India
Behzad Nematollahi, Australia

Chayut Ngamkhanong (iD), Thailand
Trung Ngo, Australia
Tengfei Nian, China
Mehdi Nikoo (iD), Canada
Youjun Ning (iD), China
Olugbenga Timo Oladinrin (iD), United Kingdom
Oladimeji Benedict Olalusi, South Africa
Timothy O. Olawumi (iD), Hong Kong
Alejandro Orfila (iD), Spain
Maurizio Orlando (iD), Italy
Siti Aminah Osman, Malaysia
Walid Oueslati (iD), Tunisia
SUVASH PAUL (iD), Bangladesh
John-Paris Pantouvakis (iD), Greece
Fabrizio Paolacci (iD), Italy
Giuseppina Pappalardo (iD), Italy
Fulvio Parisi (iD), Italy
Dimitrios G. Pavlou (iD), Norway
Daniele Pellegrini (iD), Italy
Gatheeshgar Perampalam (iD), United Kingdom
Daniele Perrone (iD), Italy
Giuseppe Piccardo (iD), Italy
Vagelis Plevris (iD), Qatar
Andrea Pranno (iD), Italy
Adolfo Preciado (iD), Mexico
Chongchong Qi (iD), China
Yu Qian, USA
Ying Qin (iD), China
Giuseppe Quaranta (iD), Italy
Krishanu ROY (iD), New Zealand
Vlastimir Radonjanin, Serbia
Carlo Rainieri (iD), Italy
Rahul V. Ralegaonkar, India
Raizal Saifulnaz Muhammad Rashid, Malaysia
Alessandro Rasulo (iD), Italy
Chonghong Ren (iD), China
Qing-Xin Ren, China
Dimitris Rizos (iD), USA
Geoffrey W. Rodgers (iD), New Zealand
Pier Paolo Rossi, Italy
Nicola Ruggieri (iD), Italy
JUNLONG SHANG, Singapore

Nikhil Saboo, India
Anna Saetta, Italy
Juan Sagaseta (iD), United Kingdom
Timo Saksala, Finland
Mostafa Salari, Canada
Ginevra Salerno (iD), Italy
Evangelos J. Sapountzakis (iD), Greece
Vassilis Sarhosis (iD), United Kingdom
Navaratnarajah Sathiparan (iD), Sri Lanka
Fabrizio Scozzese (iD), Italy
Halil Sezen (iD), USA
Payam Shafigh (iD), Malaysia
M. Shahria Alam, Canada
Yi Shan, China
Hussein Sharaf, Iraq
Mostafa Sharifzadeh, Australia
Sanjay Kumar Shukla, Australia
Amir Si Larbi (iD), France
Okan Sirin (iD), Qatar
Piotr Smarzewski (iD), Poland
Francesca Sollecito (iD), Italy
Rui Song (iD), China
Tian-Yi Song, Australia
Flavio Stochino (iD), Italy
Mayank Sukhija (iD), USA
Piti Sukontasukkul (iD), Thailand
Jianping Sun, Singapore
Xiao Sun (iD), China
T. Tafsirojjaman (iD), Australia
Fujiao Tang (iD), China
Patrick W.C. Tang (iD), Australia
Zhi Cheng Tang (iD), China
Weerachart Tangchirapat (iD), Thailand
Xiaxin Tao, China
Piergiorgio Tataranni (iD), Italy
Elisabete Teixeira (iD), Portugal
Jorge Iván Tobón (iD), Colombia
Jing-Zhong Tong, China
Francesco Trentadue (iD), Italy
Antonello Troncone, Italy
Majbah Uddin (iD), USA
Tariq Umar (iD), United Kingdom
Muahmmad Usman, United Kingdom
Muhammad Usman (iD), Pakistan
Mucteba Uysal (iD), Turkey

Ilaria Venanzi , Italy
Castorina S. Vieira , Portugal
Valeria Vignali , Italy
Claudia Vitone , Italy
Liwei WEN , China
Chunfeng Wan , China
Hua-Ping Wan, China
Roman Wan-Wendner , Austria
Chaohui Wang , China
Hao Wang , USA
Shiming Wang , China
Wayne Yu Wang , United Kingdom
Wen-Da Wang, China
Xing Wang , China
Xiuling Wang , China
Zhenjun Wang , China
Xin-Jiang Wei , China
Tao Wen , China
Weiping Wen , China
Lei Weng , China
Chao Wu , United Kingdom
Jiangyu Wu, China
Wangjie Wu , China
Wenbing Wu , China
Zhixing Xiao, China
Gang Xu, China
Jian Xu , China
Panpan , China
Rongchao Xu , China
HE YONGLIANG, China
Michael Yam, Hong Kong
Hailu Yang , China
Xu-Xu Yang , China
Hui Yao , China
Xinyu Ye , China
Zhoujing Ye , China
Gürol Yildirim , Turkey
Dawei Yin , China
Doo-Yeol Yoo , Republic of Korea
Zhanping You , USA
Afshar A. Yousefi , Iran
Xinbao Yu , USA
Dongdong Yuan , China
Geun Y. Yun , Republic of Korea

Hyun-Do Yun , Republic of Korea
Cemal YİĞİT , Turkey
Paolo Zampieri, Italy
Giulio Zani , Italy
Mariano Angelo Zanini , Italy
Zhixiong Zeng , Hong Kong
Mustafa Zeybek, Turkey
Henglong Zhang , China
Jiupeng Zhang, China
Tingting Zhang , China
Zengping Zhang, China
Zetian Zhang , China
Zhigang Zhang , China
Zhipeng Zhao , Japan
Jun Zhao , China
Annan Zhou , Australia
Jia-wen Zhou , China
Hai-Tao Zhu , China
Peng Zhu , China
QuanJie Zhu , China
Wenjun Zhu , China
Marco Zucca, Italy
Haoran Zuo, Australia
Junqing Zuo , China
Robert Černý , Czech Republic
Süleyman İpek , Turkey

Contents

Research Article

Semi-automated Generation of Geometric Digital Twin for Bridge Based on Terrestrial Laser Scanning Data

Kaixin Hu (ID),[1] **Daguang Han** (ID),[2] **Guocheng Qin** (ID),[3] **Yin Zhou** (ID),[4] **Long Chen,**[5] **Chunli Ying,**[1] **Tong Guo,**[2] **and Yanhui Liu**[6]

[1]*Chongqing Smart City and Sustainable Development Academy, Chongqing 401135, China*
[2]*School of Civil Engineering, Southeast University, Nanjing 211100, China*
[3]*Cadastral Investigation Institute, Chongqing Institute of Surveying and Monitoring for Planning and Natural Resources, Chongqing 401147, China*
[4]*Department of Civil Engineering, Chongqing Jiaotong University, Chongqing 400074, China*
[5]*College of Architecture and Civil Engineering, Loughborough University, Loughborough LE113TU, UK*
[6]*School of Civil Engineering, Southwest Jiaotong University, Chengdu 610000, China*

Correspondence should be addressed to Daguang Han; daguangh@oslomet.no

Digital twins (DTs) have a great potential for bridge operation and maintenance. Geometric digital twins (gDTs) are the key component of DTs. At present, a growing number of researchers are using high-precision 3D laser point clouds to generate gDTs. However, for large bridges, such as arch, cable-stayed, and suspension bridges, comprehensive point-cloud collection stations are difficult to set up due to their large span, narrow site, and limited field of vision. Consequently, the complete point clouds of these bridges cannot be easily obtained. Thus, knowing how to process absence point clouds and generate gDTs is an urgent problem. This study proposes a semiautomatic method of extracting geometric information of a bridge's components in the absence of point clouds. First, an algorithm based on the combination of the iterative polynomial fitting curve and sliding window is developed to extract the arch ring accurately. Second, an improved random sample consensus (RANSAC) algorithm based on distribution density is adopted to extract the cross sections of the arch bridge components, except the arch ring. For cross sections that lack point clouds, a translation strategy is used to supplement the unknown line segment. Finally, for the T-beam, a model alignment method is proposed to best match the characteristic intersections extracted by the improved RANSAC algorithm and the points corresponding to the design model. The quality of the generated models is gauged using a point cloud deviation chromatogram. In addition, the stressed component piers are compared with its design parameters to verify the accuracy of the proposed method. Results show that our method can efficiently and accurately extract geometric information and generate gDT for the bridge.

1. Introduction

Bridge safety has become a common research topic because bridges are an important part of highway infrastructure and are exposed to many dangers during their lifecycle [1]. After a bridge is built and used, knowing how to manage and maintain them is a long and costly task. Previous studies have proven that operation and maintenance costs account for half of the total costs of bridges in their lifecycle [2].

An essential problem in the operation and maintenance of bridges is efficient data storage. Nevertheless, the emergence of digital twins (DTs) has provided an effective approach to address this problem. DTs are digital copies of real-world assets [3], consisting of a 3D geometric digital twin (gDT) and semantic, material, and mechanical information. Among them, gDT is the key component. In the bridge design stage, engineers build 3D models of a bridge design according to 2D drawings. However, differences exist between the designed 3D model and gDT due to deviations

in construction [4]. To obtain gDTs, the appearance and process of a bridge and the corresponding data should be tested upon bridge completion and during its operation [5]. Building information modeling (BIM) is an effective approach of realizing parametric modeling, and it is particularly suitable for generating gDTs.

Terrestrial laser scanning (TLS) is an advanced technology used to obtain building information quickly. TLS has surpassed some traditional measurement methods [6]. Furthermore, TLS can accurately and comprehensively obtain the surface points (i.e., point clouds) of a detected object. However, TLS is mainly used to obtain and process the information of simple components, such as buildings, pipelines, and simple supported beams [7–10]. Most of these objects have simple or single components; thus, some methods are unsuitable for directly analyzing bridge components. In recent years, relevant research on bridge measurement and modeling using TLS has been conducted. Given its simple structure and wide distribution, simply supported beam bridges have become a main research object of bridge point clouds. Lu and Brilakis [11] delivered a slicing-based object fitting method that can generate the gDT of an existing reinforced concrete bridge from four types of labeled point clusters. An average modeling distance of 7.05 cm of gDT was obtained. Qin et al. [12] proposed an automatic method of reconstructing parameterized BIM by using point clouds to target simply supported beam bridges, and the accuracy was within 2 cm. For arch bridges with a complex structure, point clouds have more advantages than traditional total station measurement. Yang et al. [13] used an iterative polynomial algorithm to fit the arch structure alignment in the laboratory and obtained data of thirteen epochs. Results showed the reliability of 3D laser scanning and its advantages over traditional methods. Riveiro et al. [14] presented a new method for fully automated point cloud segmentation of masonry arch bridges. The method efficiently created segmented, spatially related, and organized point clouds, each containing relevant geometric data for a particular component (pier, arch, spandrel wall, etc.) of the structure. Occlusions and areas of low point density can cause elements to be missed or classified as noise. To address the problems that most existing methods for creating as-built BIMs from laser scanning data involve plenty of manual work, Yang et al. [15] conducted semi-automated generation of parametric BIM based on TLS data for complex steel structures. The authors believed that future research is needed to extend the developed technology to other common types of structural components, such as L-shaped components, T-shaped components, and other components formed by combining basic primitives.

TLS has great potential in the research of long-span arch bridges. First, with the arch ring as the main force-bearing object of arch bridges, the existing methods are not accurate enough for its local details. Furthermore, for large bridges, such as arch, cable-stayed, and suspension bridges, comprehensive data collection stations are difficult to set up because of their large span, narrow site, and limited field of vision. Therefore, complete point clouds are also difficult to obtain. Knowing how to process data and generate gDT in

the absence point clouds is an urgent problem. Thus, this study proposes a method of processing the absence point clouds and gDT generation. The main contributions of this method are as follows: (1) an algorithm based on the combination of the iterative polynomial fitting curve and the sliding window is developed to extract the arch ring accurately. (2) An improved random sample consensus (RANSAC) algorithm based on distribution density is adopted to extract the cross sections of arch bridge components except the arch ring. (3) Finally, for the T-beam, a model alignment method is proposed to best match the characteristic intersections extracted by the improved RANSAC algorithm and the points corresponding to the design model. The quality of the generated models is gauged using a point cloud deviation chromatogram. In addition, the stressed component piers are compared with its design parameters to verify the accuracy of the proposed method. Three algorithms are used to extract the geometric information of the arch bridge components, and the arch bridge gDT is parameterized using BIM software.

The remainder of this paper is organized as follows: Section 2 provides the research background with respect to the three aspects of bridge gDT generation: shape representation, geometric information extraction, and bridge gDT generation. The developed approach to extract geometry information from laser scanning data and generate gDT is described in Section 3. Section 4 presents illustrative examples to validate the proposed method and discusses the experimental results. Section 5 provides a summary and the conclusion of this study.

2. Related Work Background

The two kinds of point-cloud reverse-generation models are the 3D grid models [16] and geometric structures [17], and they are defined in accordance with curve shapes, vertical elevations, and cross sections. The former reconstruction method is simple, but it cannot be used with gDT to collect other information. The latter is an essential approach to gDT, and it generates data for logical objects that can be used to model the visualization and modification of these objects. In general, gDT generation for arch bridges consists of the following steps: (1) shape representation, (2) geometric information extraction, and (3) bridge gDT generation.

2.1. Shape Representation Method. No universal solution can describe 3D objects, and different representations have their own advantages and disadvantages. The choice of a shape representation method depends on the preferred modeling technology and the characteristics of the target object. The most commonly used shape representation methods can be divided into four categories: implicit representation, boundary representation, constructed solid geometry, and swept solid representation (SSR). Implicit representation requires mathematical formulas to represent 3D shapes, and it has the advantage of accurately describing the 3D shape of the object, i.e., whether it is a plane [18], a sphere, a ring [19], and so on. However, implicit representation can hardly

represent edges and vertices. Boundary representation provides information about each vertex, edge, and cycle, and it describes shapes by using their limits, thus overcoming the weakness of implicit representation. However, the results of boundary representation may be highly complicated due to the required high-resolution detail level [20], which is detrimental to operations and maintenance. Constructive solid geometry is a set of basic entity primitives that follow a certain "logic." A basic body can be in the form of a cuboid, cylinder, sphere, cone, and so on. The random sampling method of Schnabel et al. [19] can be used to model objects comprising five basic shapes: plane, sphere, cylinder, cone, and torus. Nguyen et al. [9] proposed the fitting of a segmented cylinder on the basis of normal region growth to segment and identify pipeline components. However, the shapes of bridge components are generally complex. The method of constructed solid geometry can be described as an idealized or simplified topology design, but bridge components, such as arch ring, cable, T-beam, are difficult to describe accurately. As a representation model, SSR creates a 3D shape by sweeping a 2D cross section along a specific path. Arch ring alignment, pier verticality, and cable sag are important parameters of bridges, and they can be described by a 3D path. In addition, most bridge components have a uniform section; thus, the cross section is fixed. Therefore, SSR is a suitable shape representation method to describe bridges [11, 12, 15].

2.2. Geometric Information Extraction. SSR includes two aspects: 2D cross section and 3D sweep path. Many studies have attempted to obtain the 2D cross section of point clouds. Ramamurthy et al. [21] extracted geometric features, such as line segments related to cross sections, from point clouds that contain noise and rough surfaces. Moreira et al. [22] used the concave packet algorithm to extract the concave hulls of a local XY plane of a slice. Laefer and Hong [23] proposed a kernel density estimation method to reconstruct the point cloud of standard steel beams in a BIM-compatible format. Zhou et al. [24] developed a parameter extraction method based on grid points to extract quickly and effectively bolt hole features. As for obtaining a 3D sweep path of point clouds, the line shape of the curve component with respect to a straight line is difficult to extract. Bauer and Polthier [25] proposed an automatic method of parametric reconstruction of a curved surface by using unorganized point sets. They applied the principle of using the moving least square method to calculate the spine curve of the pipe surface and approximate the polygon curve via the continuous arc spline. To obtain the deformation of each stage of an arch ring accurately, Yang et al. [13] defined the best-fitting surface and changed the usual order to move the polynomial surface closer to the actual point cloud.

For large bridges, such as arch, cable-stayed, and suspension bridges, comprehensive point-cloud collection stations are difficult to set up because of their large span, narrow site, and limited field of vision. Consequently, the complete point clouds of these bridges are also difficult to obtain. Knowing how to process absence point clouds and

generate gDT is an urgent problem. Yang et al. [15] extracted data from 39 pillars of a bridge for a large-scale bridge-like steel structure and completed an as-built BIM. In achieving a complete model, the modeling parameters of the two missing struts in their work and the corresponding connection plates were manually generated. The arch ring is the main bearing component of an arch bridge, and thus, ensuring its high-precision alignment is important. Knowing how to process absence point clouds is another urgent problem. Thus, an improved RANSAC algorithm based on distribution density is adopted in this study to extract the sections of arch bridge components except the arch ring. For sections that lack point clouds, the translation strategy is used to supplement the unknown line segment. For the T-beam, a model-matching algorithm is used to best align the design model and gDT.

2.3. Bridge gDT Generation. In contrast to the component model generation of bridges, that of buildings is relatively simple. Jung et al. [26] built the inner and outer walls of buildings through point cloud segmentation and feature recognition. The object of their study only included a single type of a component. Danielle et al. [27] suggested the use of a data-processing algorithm as provided by a point cloud library to create walls and floors. For the common existence of simple and complex shapes, Barazzetti et al. [28] proposed a parametric BIM generation method that can preliminarily separate two aspects. For simple shape modeling, commercial BIM software is used. For complex shape modeling, nonuniform rational basis splines are utilized. Commercial BIM software provides powerful tools for modelers, and it is the platform of choice for most modelers. Quattrini et al. [29] used Autodesk Recap and Revit to create 3D models directly from point cloud data and subsequently modeled them using parameterized elements in Revit (i.e., built-in family library and custom family). However, current experience suggests that no software can perform all geometric modeling [30].

Most software platforms support only a few standard components, such as wall and pipe modeling [31]. In addition, information may be lost due to manual modeling operations [32]. Thus, modeling efficiency is difficult to ensure [33]. In this study, the CATIA platform, which is known for its powerful parameterization ability, is adopted to generate arch bridge gDT.

3. Methods

3.1. Overview. This section describes the semi-automated generation of gDT for arch bridge based on TLS data. For large bridges, such as arch, cable-stayed, and suspension bridges, comprehensive point cloud collection stations are difficult to set up because of their large span, narrow site, and limited field of vision. Therefore, the object of this study is the absence point cloud.

Figure 1 shows an overview of our method that includes three steps: (1) data segmentation, (2) extraction of the bridge components' geometric information, and (3)
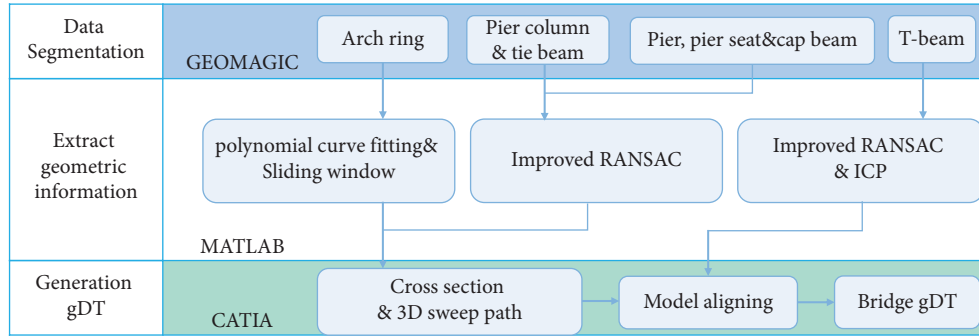
FIGURE 1: Overview of the proposed method for arch bridge gDT generation.

parametric bridge gDT generation. Section 3.2 introduces that the point cloud processing software Geomagic is used to separate different components of the arch bridge and classify them into different categories. Section 3.3 discusses the algorithms that have been developed and implemented in MATLAB for various components to extract the bridge components' geometric information. Among them, each object class has its own workflow. Section 3.4 presents the process of how to generate the parametric bridge gDT in CATIA. In this study, all solutions of bridge component generation are in SSR.

The assumptions for the shape of components are described as follows: (1) an arch ring section is an equal section, and any section is the design section size. (2) The assumption of pier column, tie beam, and so on section is that one side cannot be fitted effectively. If the corresponding parallel edge has been successfully fitted, then the translation strategy is adopted; otherwise, the design information is used for supplementation. (3) The T-beam section is consistent with the design size because the T-beam is modeled by aligning the design model with extract feature intersection points to the greatest extent using the ICP algorithm.

3.2. Data Segmentation.

After pretreating the point clouds, the arch bridge point clouds are manually divided into four categories of components in Geomagic. The manual division time of the entire bridge is approximately 15 min. The first category is the arch ring. The second category is the pier column and tie beam. The third category is the pier, pier seat, and bent cap. The fourth category is the T-beam. The arch ring is the main stress structure of the arch bridge, as depicted by the rectangular stretching along the arch axis in Figure 2(a). The quality of several piers is crucial in identifying the stress of an arch bridge. The pier column and tie beam of the arch bridge are usually rectangular section components, as shown in Figure 2(b). The pier, pier seat, and bent cap of the arch bridge can be regarded as a standard contour along a line; hence, they are divided into the same category, as shown in Figure 2(c). The T-beam is the main component of the arch bridge deck, and it has a complex shape. However, in this study, the T-beam adopts the prefabrication method and has a unified size in the bridge, as shown in Figure 2(d).

3.3. Geometric Information Extraction

3.3.1. Arch Ring. As this study adopts the SSR method, the following two elements are required: (1) 2D cross section and (2) 3D path. For the arch ring, the complete point clouds of the arch-ring cross section are difficult to obtain. Changing the cross-sectional size of the arch ring has a negligible effect on the stress of the arch bridge. Thus, the design size of the 2D cross section is adopted. The 3D path of the arch ring is crucial in handling the stress of the arch bridge, further indicating that an accurate extraction algorithm is needed. First, a similar but nonidentical polynomial curve fitting method is used to describe the initial alignment of the arch ring [13]. Second, the obtained polynomial is used as the initial parameter of the sliding window algorithm to ensure an accurate extraction.

Polynomial curve fitting should meet two requirements to achieve the optimal results. First, the standard deviation between all points and each order of the polynomial curve fitting should be less than a given value (i.e., 0.5 m). Second, the standard deviation of the polynomial curve fitting should be less than that of a higher-order polynomial curve fitting. From the standard deviations of all points and each order of the polynomial curve fitting, the best polynomial curve fitting can then be selected. Figure 3 shows the solution process of the optimal polynomial curve fitting. The materials and methods section should contain sufficient detail so that all procedures can be repeated. It may be divided into headed subsections if several methods are described.

$$z = a_n \cdot x^n + a_{n-1} \cdot x^{n-1} + \ldots + a_2 \cdot x^2 + a_1 \cdot x^2 + a_0, \qquad (1)$$

where x and z are the 2D coordinates of each point, and $a_0 - a_n$ represents the parameter to be estimated. The unknown parameters $a_0 - a_n$ are calculated using the least square method.

The specific steps of the sliding window algorithm are as follows: first, the best polynomial curve fitting is used to provide the slope of the tangent line at each interpolation point $\text{tangent}_j = f$. The normal direction is given by $\text{normal}_j = -1/\text{tangent}_j$. Then, the interval of the interpolation points is selected in accordance with the actual situation. Given the size of a long-span arch bridge, the interval is set to 1-2 m, as shown in Figure 4.
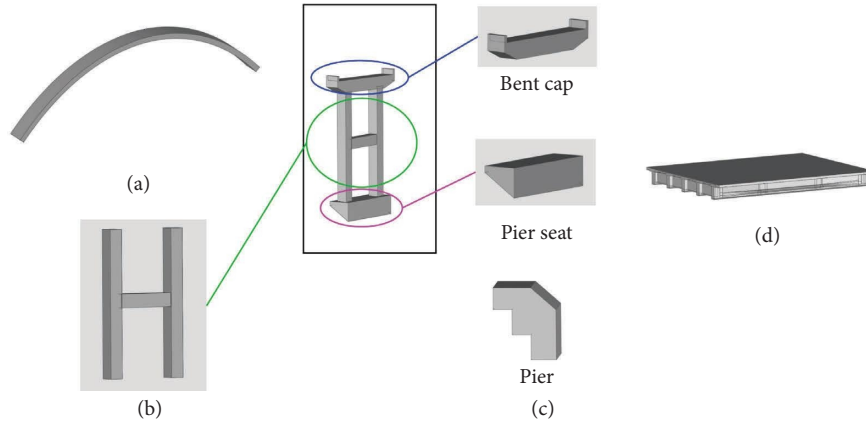
FIGURE 2: Illustrations of different components: (a) arch ring; (b) pier column and tie beam; (c) pier, pier seat, and bent cap; and (d) T-beam.
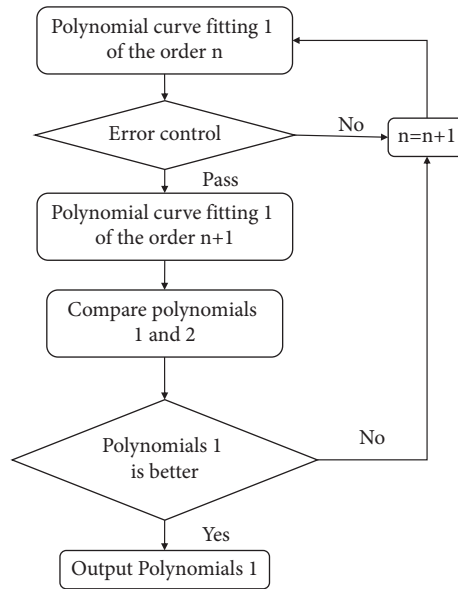
FIGURE 3: Process of the iterative polynomial fitting curve.

The rotation angle φ_j is derived from the angle between the normal direction of slice j and the global X-axis. In particular, the interpolation points of each slice j are used to calculate the normal direction of each slice. The changes in coordinates of the corresponding rotation angle $-\varphi_j$ for each window point cloud are determined as follows:

$$\begin{bmatrix} x' \\ y' \\ z' \end{bmatrix} = \begin{bmatrix} \cos\left(-\varphi_j\right) & \sin\left(-\varphi_j\right) & 0 \\ -\sin\left(-\varphi_j\right) & \cos\left(-\varphi_j\right) & 0 \\ 0 & 0 & 1 \end{bmatrix} \cdot \begin{bmatrix} x \\ y \\ z \end{bmatrix}. \qquad (2)$$

The expected value of the window point cloud can then be solved. Finally, the expected value of each window point cloud is rotated such that it is given by $-\varphi_j$. The linear control points at the bottom of the arch ring can then be obtained. The cubic spline is used for the connection.

3.3.2. Pier Column and Tie Beam. The axis is the key geometric feature of the pier column and tie beam because these components are subjected to axial force. The perpendicularity of the pier column axis is taken as the key parameter in the detection. The pier column and tie beam of an arch bridge are usually rectangular. In view of ensuring the representativeness of our method, the rectangular cross-sectional pier column with two- and three-side point clouds is selected as the research object, as shown in Figure 5(a). The point clouds of the pier are segmented via the slicing method. The specific method involves cutting the data along the Z-axis in a plane parallel to the XY plane to obtain multiple cross sections, as shown in Figure 5(b). During site construction, the pier height of each pouring is 0.5–1 m. A 0.5–1 m length in the Z-direction is recommended. An improved RANSAC algorithm based on distribution density is adopted to extract the sections of the arch bridge components except the arch ring. For the sections that lack point
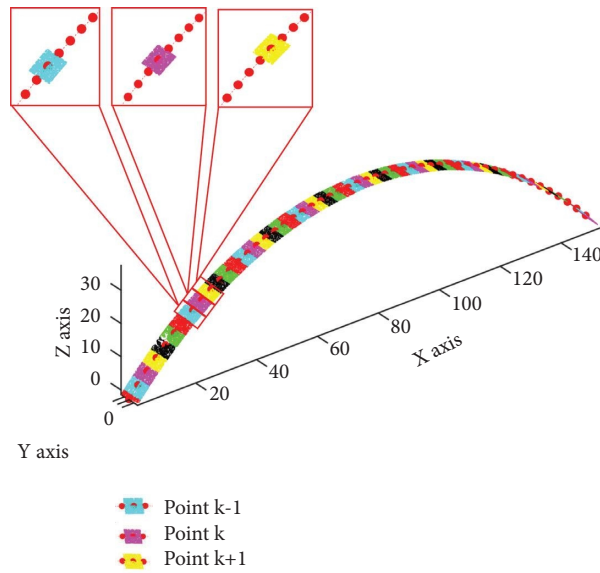
FIGURE 4: Slide window algorithm.
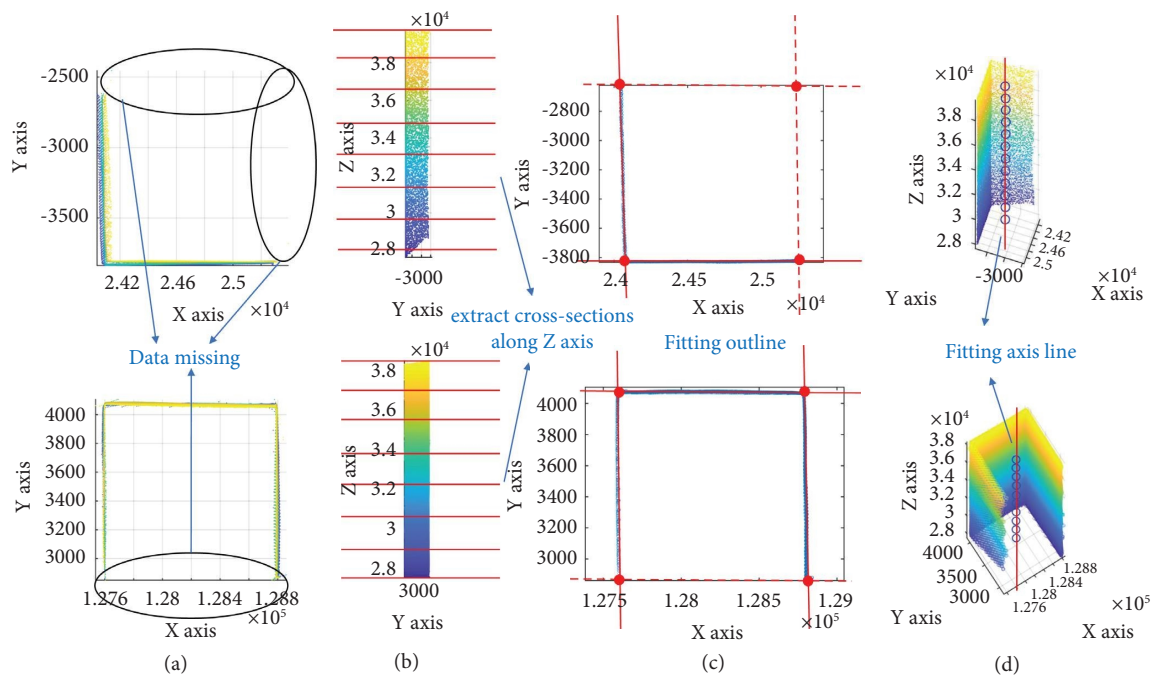
FIGURE 5: Illustrations of axis line for pier column and tie beam: (a) original point clouds, (b) extracted cross sections along the Z-axis, (c) fitting outline, and (d) fitting axis line.

clouds, the translation strategy is used to supplement the unknown line segment. Finally, the intersection of each line is obtained and then used to calculate the centroid of the intersection, as shown in Figure 5(c). The axis of the pier column is obtained via the least square method, as shown in Figure 5(d).

The specific steps of the improved RANSAC algorithm based on the distribution density algorithm are in the following steps, as shown in Figure 6. First, the number of point clouds per millimeter along the X-axis and Y-axis of each

cross-section point clouds is calculated as m, and the average density is calculated as ρ. In addition, the density threshold is defined as ρ_t. Then, when $m \geq \rho_t$, the length T corresponding to the time point cloud is used as the threshold of the algorithm.

$$\rho_t = k\rho \, (k \in (3, 5)), \tag{3}$$

where $\rho_x = N_a/a$, $\rho_y = N_b/b$; N_a and N_b represent the total number of points on the X-axis and Y-axis of the cross section, respectively; a and b represent the width and height
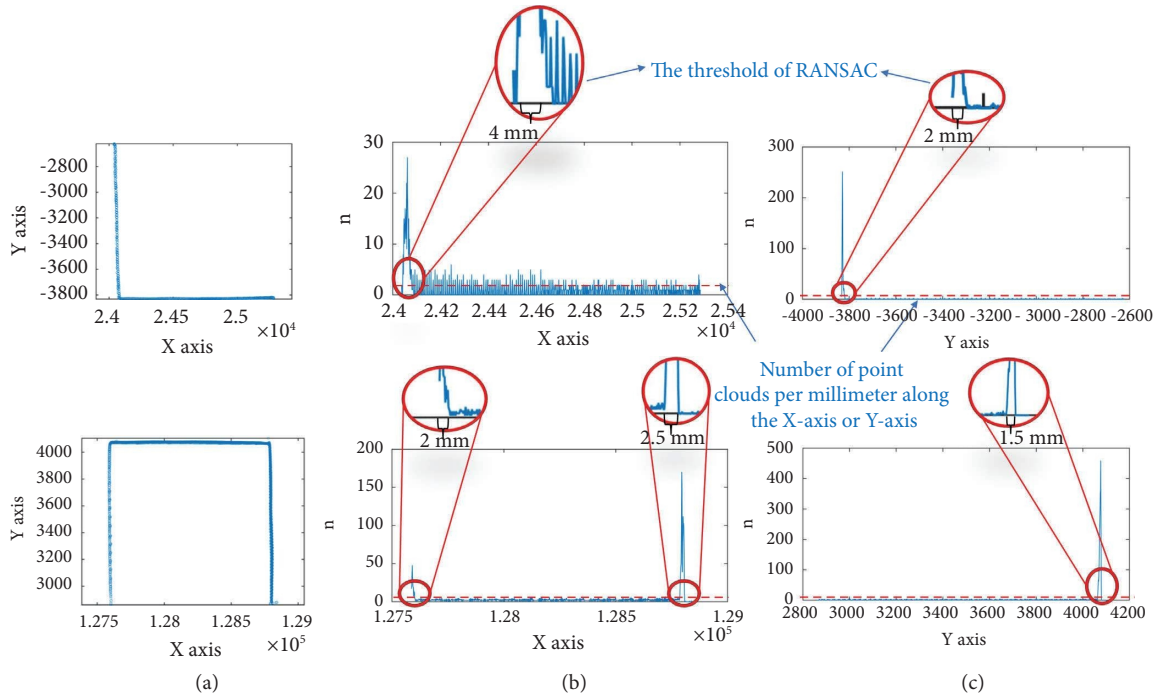
FIGURE 6: Calculation step of the threshold in RANSAC: (a) cross section of the point clouds, (b) number of point clouds per millimeter along X-axis, and (c) number of point clouds per millimeter along Y-axis.

Input: cross-sectional pier column with two-side point clouds list $Data_{n\times3}$;
Output: The improved RANSAC algorithm's Distance threshold T, the axis of the pier column $\vec{l_0}$.
    $Dataz = Data_{n\times3}$ (:, 3);
    $dz = 1000$; //Cut the interval of $Data$ along the Z-axis in a plane parallel.
    kz;//Quotient of total length of $Dataz$ and dz.
    $dx = 1$; //millimeter.
    kx;//Number of millimeters along the X-axis of each cross section.
    for $i = 1$to kz do
    $Datai$; //Obtain the Point clouds of each segment of point clouds after cutting.
    N_a, a;//N_a is the total number of points on the X-axis a of the cross section. a is the width of the cross section.
    $\rho_x = N_a/a$; //The average density is calculated ρ Along the X axis.
    $\rho_t = 3 * \rho_x$; //Definition the density threshold.
        for $j = 1$to kx do
        m_x; //Calculated the number of point clouds per millimeter along X-axis.
        end for
    Tx; //Find the number greater than ρ_t in m_x, and then the product of dx.
    Ty; //It is the same as the solution process Tx.
    $l_1 = $ RANSAC ($Data$, Tx); //Using RANSAC algorithm to fit straight line.
    $Data0$; //Delete the point cloud in $Data$ used in l_1
    $l_2 = $ RANSAC ($Data0$, Ty); //Using RANSAC algorithm to fit remaining straight line.
    $l_3 = l_1 + (0, 0, a)$; //the translation strategy is used to supplement the unknown line segment.
    $l_4 = l_2 + (0, 0, b)$; //like l_3.
    $[P_{t1}, P_{t2}, P_{t3}, P_{t4}]$; //calculate the intersection of l_1, l_2, l_3, l_4.
    P_c; //calculate the centroid of the intersection.
end for
$\vec{l_0}$; //calculate the axis of the pier column.

ALGORITHM 1: Improved RANSAC algorithm.

of the cross section, respectively. The RANSAC algorithm of threshold T is used to fit the straight line of the cross section iteratively. The specific algorithm for calculating the axis of the pier column is given in Algorithm 1.

3.3.3. Pier, Pier Seat, and Bent Cap. The pier, pier seat, and bent cap of an arch bridge can be regarded as having a standard contour along one line; thus, they can be classified in the same category. These components are not necessarily perfectly vertical; however, the piers are assumed to be quasivertical in this study. First, the piers and pier seat are projected onto the XZ plane, as shown in Figures 7(a) and 7(b). The bent cap is projected onto the XY plane, as shown in Figure 7(c). The 2D ConcaveHull α-shape [22] is used to describe the outline of the slice cross section of the point clouds. Similarly, the improved RANSAC algorithm in Section 3.3.2 is adopted to extract the sections. In particular, their point clouds are absent because of the shielding of the soil around the pier and the diminutive size of the stops, which are similar to those of the pier column and tie beam, on both sides of the bent cap.

3.3.4. T-Beam. Most beam–slab bridges use precast concrete members as the main structural members [34]. The T-beam of an arch bridge is the same. The superstructure of arch bridges is the same as that of beam–slab bridges. Usually, the point clouds on both sides of the T-beam are difficult to determine, hence the incomplete data. Therefore, the point clouds of one side of the T-beam are selected in this research. The T-beam entails a complex modeling, further suggesting the inapplicability of the translation strategy.

The point clouds of the pier are segmented via the slicing method. In particular, the data along the X-axis in a plane parallel to the YZ plane are cut to obtain multiple cross sections, as shown in Figure 8 (a). A 0.5–1 mm length in the X-direction is recommended. The improved RANSAC algorithm based on distribution identity is used to obtain some characteristic intersections of the T-beams. And the calculated threshold of the improved RANSAC is shown in 8 (b). The characteristic intersections of each T-beam section total four, as shown in Figure 8 (c). The model alignment algorithm is proposed to best match the characteristic intersections extracted by the improved RANSAC algorithm and the points corresponding to the design model. For the T-beam, a model-aligning algorithm is proposed. In particular, the outline of some characteristic intersections of T-beams is obtained. Then, the iterative closest point (ICP) algorithm is used to match characteristic intersections and the points corresponding to the design model.

3.4. Bridge gDT Generation. After geometric information of the components is extracted as derived from the point clouds, it is stored in an Excel file. By automatically assigning the coordinates stored in Excel to the corresponding PART module of CATIA, the arch bridge gDT can also be

established in CATIA. The three steps of this approach can be described as follows:

Step 1 : Generation of the arch bridge skeleton. Except for the T-beam characteristic intersections, the skeleton includes the 3D path and projection plane of the other components. First, the coordinate system of the entire arch bridge is determined through an approach that is essentially the same as that of the construction coordinate system. Then, the information is imported into CATIA's PART module, as shown in Figure 9(a).

Step 2 : Generation of the templates for each component. First, the local coordinate system is created in the PART module of CATIA. The Z-axis is in the 3D path, which is defined as a straight line or a curve. The X- and Y-axes should conform to the principles of the Cartesian coordinate system. Then, the origin of the component is determined. For the arch ring, pier, and tie beam, the origin is the center point of the profile. For the pier, pier seat, bent cap, and T-beam, the origin is the corner of the profile. Finally, the corners of the cross section are sketched and then connected with the segments, as shown in Figure 9(b).

Step 3 : Lofting of each component. The generation component templates are lofted on the arch bridge skeleton, as shown in Figure 9(c).

4. Experiments

4.1. Point Cloud Acquisition and Processing. The proposed semiautomatic method for extracting the geometric information of the bridge's components in the absence of point clouds was verified in this study. We used a Leica 3D laser scanner to collect the point clouds of a long-span arch bridge. The vertical and horizontal fields of view of the scanner were 300° and 360°, respectively. The distance between two points at a distance of 10 m in the resolution gear was approximately 3 mm, and the data collection time of each scan was approximately 13 minutes. Similar to the stations of cable-stayed and suspension bridges, the comprehensive data collection stations in this study were difficult to set up because of the model's large span, narrow site, and limited field of vision. In accordance with the actual situation of the bridge, three stations must be set up to obtain the required point clouds in Figure 10 (a). The point clouds of the three stations were registered using the ICP algorithm in CloudCompare software, as shown in Figure 10 (b). Among them, the first station was considered the target station. A total of 48,300 points in the joint station of the second and first stations were processed, and the final RMS was 0.0021 m. In addition, a total of 42,380 points in the third and first stations were processed, and the final RMS was 0.0018 m. To ensure the accuracy of
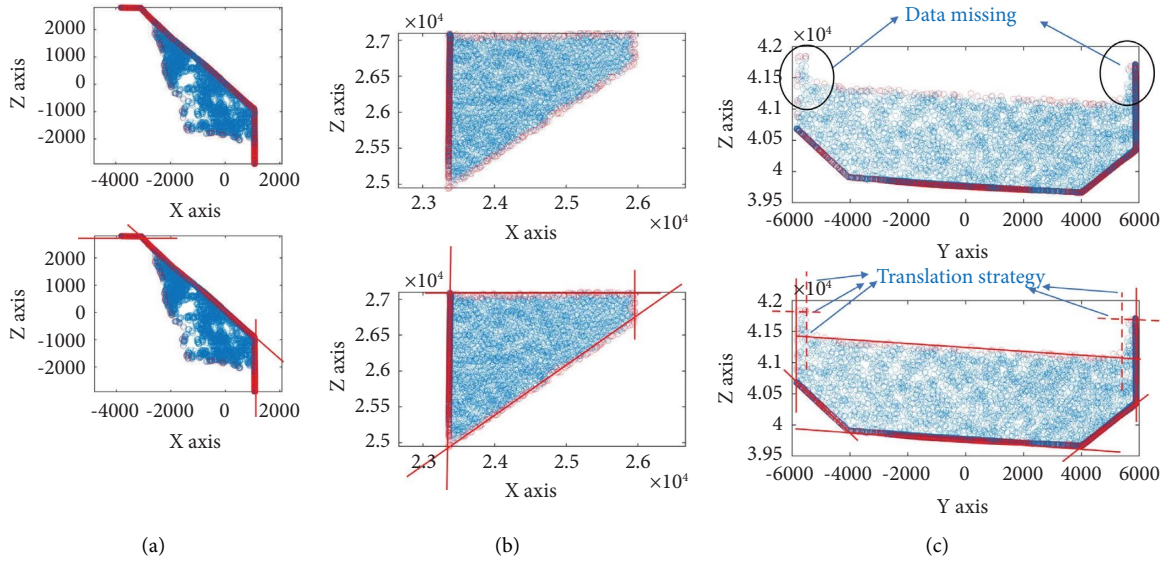
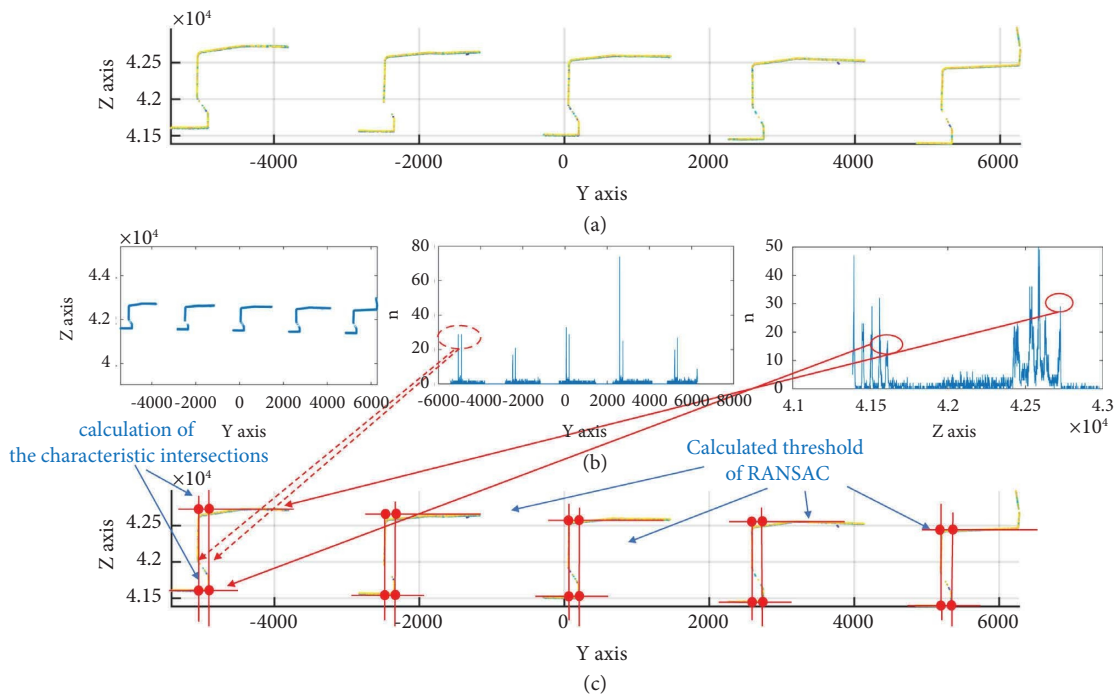FIGURE 7: Illustrations of cross section: (a) pier, (b) pier seat, and (c) bent cap.

FIGURE 8: Illustrations of characteristic intersections for T-beam: (a) original point clouds, (b) calculated threshold of RANSAC, and (c) calculation of the characteristic intersections.
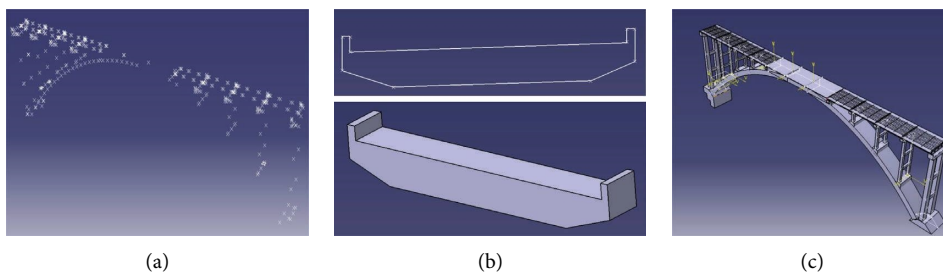

FIGURE 9: Illustration of gDT generation: (a) generation of the arch bridge skeleton, (b) generation templates for component, and (c) lofting of each component.
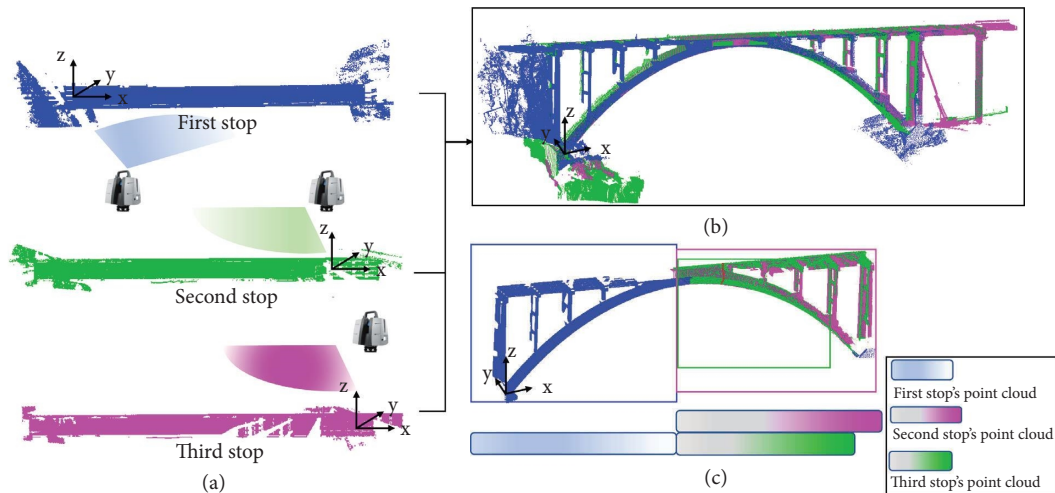
FIGURE 10: Illustration of gDT generation: (a) arch bridge scanning, (b) station processed by the ICP algorithm, and (c) point cloud used for generating gDT.

gDT generation, only about half of the point clouds in each station were selected in Figure 10 (c).

First, the Geomagic software is used for data segmentation and data format conversion. The bridge was composed of an arch ring, 16 pier columns, 12 tie beams, two piers, 16 pier seats, eight bent caps, and 10 span T-beams. These components were manually separated and saved as .txt files, including the X, Y, and Z coordinates of each point. Then, each txt file was imported into MATLAB to execute the algorithms developed for the different components. The creation sequence was in the order of arch ring, pier column, tie beam, pier, pier seat, bent cap, and T-beam.

4.2. Results. The method described in Section 3.4 was used to generate the gDT of the arch bridge. To check the original coordinate matching degree between the gDT and its point clouds, we converted the point clouds before segmentation and the reconstructed CATIA model into STP format and then imported them into Geomagic. We imported the bridge point clouds before segmentation, followed by the gDT of the arch bridge, into Geomagic. Figure 11 shows the coincidence of the two components and the deviation chromatogram of the arch ring, pier column, tie beam, pier, pier seat, bent cap, and T-beam. The deviation between the point clouds of some components and their gDT was evenly distributed, and most of them were within 5 mm.

Except for the absence point cloud, most other point clouds and their gDT coincide with each other, as illustrated in Figure 11. Some deviations can be observed in some parts of each component. This phenomenon can be attributed to three reasons: (1) the small amount of noise in the point clouds, (2) the format conversion between models in the

software, and (3) the error of the cross-sectional fitting algorithm.

The arch ring linear is critical to the mechanical performance of the arch bridge. Taking the actual point cloud as a reference, the results of distance deviation between the polynomial curve fitting and the algorithm in this paper are compared. Among them, the root mean square error (RMSE) of the polynomial fitting curve algorithm is 0.0126 m, and the RMSE of the algorithm in this paper is 0.0055 m, which indicates that the latter is better in fitting the arch line. Among them, there are several obvious abnormalities in the distance deviation of the polynomial fitting curve algorithm, such as the midspan and quarter of the arch ring as depicted in Figure 12. The enlarged index of these corresponding positions shows that, compared with the control points of the algorithm in this paper are closer to the point cloud, the alignment of the polynomial fitting curve algorithm is farther from the point cloud, which further illustrates the progress of the algorithm in this paper.

In addition, the quality of the pier columns is important to the arch bridge. Here, the geometric information of the extracted pier column was compared with the design information in the construction drawing in two aspects: (1) intersection of the pier column centerline and pier base horizontal line and (2) perpendicularity. The results showed that the deviation of the intersection relative to the design intersection has a normal distribution. Moreover, the RMSE of the deviation was 0.0041 m, as depicted in Figure 13. The deviation between the perpendicularity of the pier column and the design angle in terms of RMSE was 0.046°, as shown in Figure 14. According to Klein et al. [35], an error of approximately 2% is acceptable in the as-built BIM model facility management.
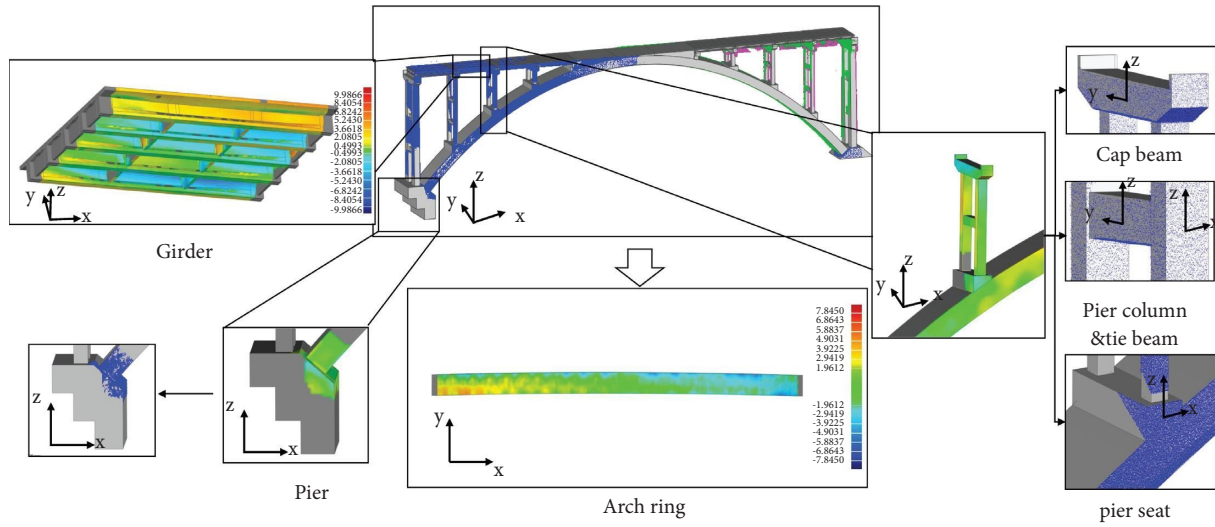
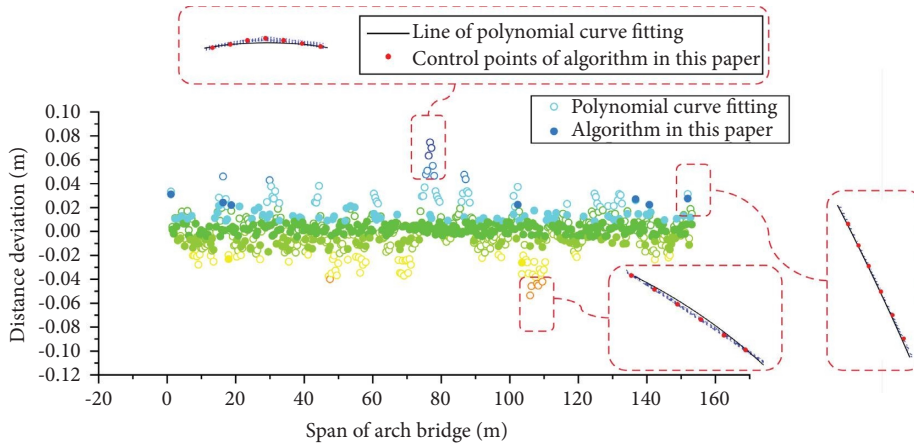FIGURE 11: Deviation chromatogram of the arch bridge components, unit: mm.

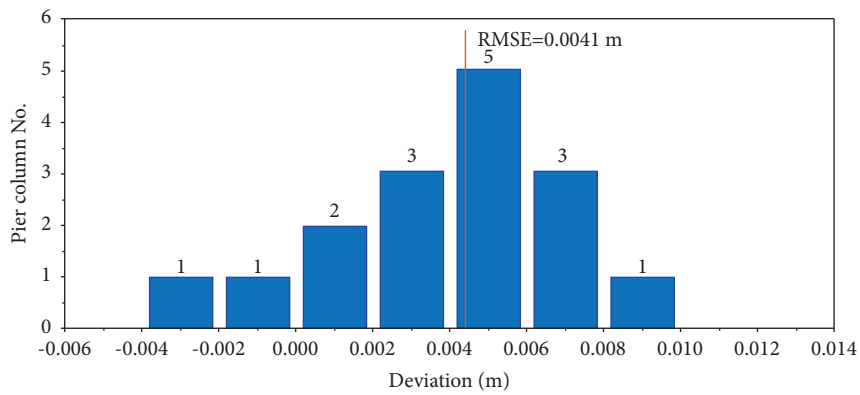FIGURE 12: Accuracy analysis of arch ring linear algorithm.

FIGURE 13: Deviation of the intersection relative to the design intersection.
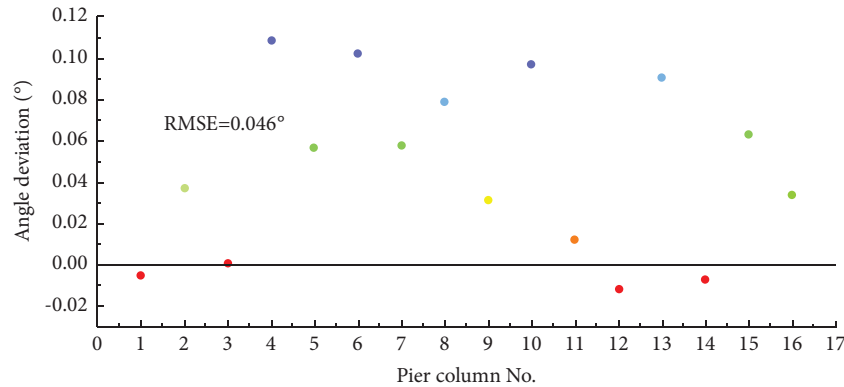
Figure 14: Deviation between the perpendicularity of the pier column and the design angle.

5. Conclusions and Prospect

This study proposed a semiautomatic method to extract geometric information of bridge components in the absence of point clouds. The arch bridge components included the arch ring, pier column, tie beam, pier, pier seat, bent cap, and T-beams. Geometric information was extracted from point clouds, and it included the following: arch ring alignment; centerline and contour of the pier column and tie beam; contour of the pier, pier seat, and bent cap; and feature points that match the T-beam. After the geometric information of each structural member from the point clouds was extracted, information was stored in an Excel file. The coordinates stored in Excel were automatically assigned to the corresponding module of CATIA, and the gDT of the arch bridge was generated in CATIA.

The method was verified on a large-arch bridge. During geometric information extraction, the arch ring, 16 pier columns, 12 tie beams, two piers, 16 pier seats, eight bent caps, and 10 prefabricated box girders of the arch bridge were successfully extracted. The deviation between the point cloud and the gDT model of the reconstructed bridge was distributed in Geomagic. The deviation chromatogram showed that the deviation between the point cloud of each component and the gDT model of the reconstructed bridge was evenly distributed, and most of them were within 5 mm. Subsequently, the geometric information of various pier columns was compared with the design information in the construction drawings in two aspects: (1) intersection of the pier column centerline and pier seat horizontal line and (2) perpendicularity. Results show that the deviation of the intersection relative to the design intersection entailed a normal distribution. Furthermore, the RMSE of the deviation was 0.0041 m. Results also indicate that our method can accurately extract the geometric features of arch bridge components from the point cloud data of arch bridges with defects.

Compared with traditional methods, the innovation in this study can be summarized as follows: first, the algorithm in this paper combines the advantages of the iterative polynomial algorithm and the sliding window algorithm, which can obtain a more accurate and stable fitting of the local alignment of the arch bridge compared with the traditional algorithm. Second, for the cross section of components with missing point clouds, the improved RANSAC algorithm uses a translation strategy to supplement unknown line segments to extract the characteristics of components. Third, researchers suggested using a template matching method to find the best match girder type in existing forecast bridge beam catalogues due to the complexity of the T-beam [15]. Three criteria for model matching include (1) span length, (2) girder bottom flange, and (3) web depth. The database is the standard product of the American Association of State Highway and Transportation Officials and the Bridge Beam Manual provided by BANAGHER Precast Concrete. However, a particularly accurate T-beam model may not be found due to the limitation of the database. The proposed algorithm in this paper can be applied to any T-beam to best match the design model and characteristic intersections.

Although this study shows promising results, certain limitations should be addressed. First, most of the cross-sectional forms of bridge members in this study were composed of multiple straight lines. Future research may extend the algorithm to other common types of member sections, such as the circular section and the section composed of multiple curve segments. Second, our method involved a manual segmentation process. Future studies may focus on local feature detection and other methods to segment various components automatically and improve the efficiency of data processing. Finally, gDT models should be able to handle additional mechanical information to realize the establishment of DTs further.

Data Availability

The data used to support the findings of this study are available from the corresponding author upon request.

Conflicts of Interest

The authors declare that there are no conflicts of interest regarding the publication of this paper.

References

[1] J. M. Andrić and D. G. Lu, "Risk assessment of bridges under multiple hazards in operation period," *Safety Science*, vol. 83, pp. 80–92, 2016.

[2] D. M. Baker and M. Cullimore, "Operation and maintenance of the clifton suspension bridge," *Europhysics News*, vol. 44, no. 2, pp. 16–20, 2015.

[3] A. Parrott and W. Lane, *Industry 4.0 and the Digital Twin*, Deloitte University Press, NY, US, 2017.

[4] R. Lopez and P. E. D. Love, "Design error costs in construction projects," *Journal of Construction Engineering and Management*, vol. 138, no. 5, pp. 585–593, 2012.

[5] D. Honfi, I. Bjornsson, O. L. Ivanov, and J. Leander, "Informed successive condition assessments in bridge maintenance," *Journal of Civil Structural Health Monitoring*, vol. 10, no. 4, pp. 729–737, 2020.

[6] V. Kankare, M. Holopainen, M. Vastaranta et al., "Individual tree biomass estimation using terrestrial laser scanning," *ISPRS Journal of Photogrammetry and Remote Sensing*, vol. 75, no. 1, pp. 64–75, 2013.

[7] M. Hochmuth, "Parameterized bridge design - conceptual, preliminary and detailed design," *Bautechnik*, vol. 93, no. 3, pp. 162–169, 2016.

[8] C. Wang, Y. K. Cho, and C. Kim, "Automatic BIM component extraction from point clouds of existing buildings for sustainability applications," *Automation in Construction*, vol. 93, no. 3, pp. 1–13, 2015.

[9] C. H. P. Nguyen and Y. Choi, "Comparison of point cloud data and 3D CAD data for on-site dimensional inspection of industrial plant piping systems," *Automation in Construction*, vol. 91, pp. 44–52, 2018.

[10] H. M. Lee and H. S. Park, "Gage-free stress estimation of a beam-like structure based on terrestrial laser scanning," *Computer-Aided Civil and Infrastructure Engineering*, vol. 26, no. 8, pp. 647–658, 2011.

[11] R. Lu and I. Brilakis, "Digital twinning of existing reinforced concrete bridges from labelled point clusters," *Automation in Construction*, vol. 105, pp. 102837–102837 16, 2019.

[12] G. Qin, Y. Zhou, K. Hu, D. Han, and C. Ying, "Automated reconstruction of parametric BIM for bridge based on terrestrial laser scanning data," *Advances in Civil Engineering*, vol. 2021, pp. 1–17, 2021.

[13] H. Yang, X. Y. Xu, and I. Neumann, "Deformation behavior analysis of composite structures under monotonic loads based on terrestrial laser scanning technology," *Composite Structures*, vol. 183, pp. 594–599, 2018.

[14] B. Riveiro, M. J. Dejong, and B. Conde, "Automated processing of large point clouds for structural health monitoring of masonry arch bridges," *Automation in Construction*, vol. 72, pp. 258–268, 2016.

[15] L. Yang, J. C. Cheng, and Q. Wang, "Semi-automated generation of parametric BIM for steel structures based on terrestrial laser scanning data," *Automation in Construction*, vol. 112, Article ID 103037, 2020.

[16] C. Thomson and J. Boehm, "Automatic geometry generation from point clouds for BIM," *Remote Sensing*, vol. 7, no. 9, pp. 11753–11775, 2015.

[17] W. F. Chen and L. Duan, *Bridge Engineering Handbook: Construction and Maintenance, Bridge Engineering*, Springer, Berlin, Germany, 2014.

[18] F. A. Limberger and M. M. Oliveira, "Real-time detection of planar regions in unorganized point clouds," *Pattern Recognition*, vol. 48, no. 6, pp. 2043–2053, 2015.

[19] R. Schnabel, R. Wahl, and R. Klein, "Efficient RANSAC for point-cloud shape detection," *Computer Graphics Forum*, vol. 26, no. 2, pp. 214–226, 2007.

[20] J. Chen, C. Zhang, and P. Tang, "Geometry-based optimized point cloud compression methodology for construction and infrastructure management," in *Proceedings of the ASCE International Workshop on Computing in Civil Engineering*, pp. 377–385, IEEE, Seattle, WA, USA, June 2017.

[21] R. Ramamurth, K. Harding, and X. Du, "Geometric and topological feature extraction of linear segments from 2D cross-section data of 3D point clouds," *SPIE Sensing Technology Applications*, vol. 9489, pp. 236–247, 2015.

[22] A. J. C. Moreira and M. Y. Santos, "Concave hull: a k-nearest neighbours approach for the computation of the region occupied by a set of points," in *Proceedings of the GRAPP 2007 Second International Conference on Computer Graphics Theory and Applications GM/R. DBLP*, IEEE, Barcelona, Spain, March 2007.

[23] D. F. Laefer and L. Truong-Hong, "Toward automatic generation of 3D steel structures for building information modelling," *Automation in Construction*, vol. 74, pp. 66–77, 2017.

[24] Y. Zhou, D. Han, K. Hu et al., "Accurate virtual trial assembly method of prefabricated steel components using terrestrial laser scanning," *Advances in Civil Engineering*, vol. 2021, no. 15, pp. 1–15, 2021.

[25] U. Bauer and K. Polthier, "Generating parametric models of tubes from laser scans," *Computer-Aided Design*, vol. 41, no. 10, pp. 719–729, 2009.

[26] J. Jung, C. Stachniss, S. Ju, and J. Heo, "Automated 3D volumetric reconstruction of multiple-room building interiors for as-built bim," *Advanced Engineering Informatics*, vol. 38, no. 10, pp. 811–825, 2018.

[27] T. K. Danielle, E. N. Tchinda, and C. Bobda, "From PC2BIM: automatic model generation from indoor point cloud," in *Proceedings of the 13th International Conference on Distributed Smart Cameras*, vol. 23, IEEE, New York, NY, USA, September 2019.

[28] L. Barazzetti, F. Banfi, and R. Brumana, "BIM from Laser Clouds and Finite Element Analysis: Combining Structural Analysis and Geometric Complexity," *International Archives of the Photogrammetry Remote Sensing and Spatial Information Sciences*, vol. 40, pp. 345–350, 2015.

[29] R. Quattrini, E. S. Malinverni, P. Clini, R. Nespeca, and E. Orlietti, "From TLS to HBIM: high quality semantically-aware 3D modeling of complex architecture," *The International Archives of the Photogrammetry, Remote Sensing and Spatial Information Sciences*, pp. 367–374, 2015.

[30] P. Tang, D. Huber, B. Akinci, R. Lipman, and A. Lytle, "Automatic reconstruction of as-built building information models from laser-scanned point clouds: a review of related techniques," *Automation in Construction*, vol. 19, no. 7, pp. 829–843, 2010.

[31] E. Agapaki and I. Brilakis, "State-of-Practice on As-Is Modelling of Industrial Facilities S," *Advanced Computing Strategies for Engineering*, pp. 103–124, 2018.

[32] H. Son, F. Bosche, and C. Kim, "As-built data acquisition and its use in production monitoring and automated layout of civil infrastructure: a survey," *Advanced Engineering Informatics*, vol. 29, no. 2, pp. 172–183, 2015.

[33] E. Hoffman, "Specifying laser scanning services," *Chemical Engineering Progress*, vol. 101, no. 5, pp. 34–38, 2005.

[34] M. K. Kim, S. McGovern, M. Belsky, C. Middleton, and I. Brilakis, "A suitability analysis of precast components for standardized bridge construction in the United Kingdom," *Procedia Engineering*, vol. 164, pp. 188–195, 2016.

[35] L. Klein, N. Li, and B. Becerik-Gerber, "Imaged-based verification of as-built documentation of operational buildings," *Automation in Construction*, vol. 21, pp. 161–171, 2012.

Research Article

Digital Twin-Based Investigation of a Building Collapse Accident

Zhe Zheng [ID],[1] **Wenjie Liao** [ID],[1] **Jiarui Lin** [ID],[1] **Yucheng Zhou** [ID],[1] **Chi Zhang,**[1,2] **and Xinzheng Lu** [ID][1]

[1]*Key Laboratory of Civil Engineering Safety and Durability of Ministry of Education, Tsinghua University, Beijing, China*
[2]*China Southwest Architectural Design and Research Institute Corporation Ltd., Chengdu, China*

Correspondence should be addressed to Xinzheng Lu; luxz@tsinghua.edu.cn

The collapse of engineering structures can cause significant casualties and have negative social effects. Collapse accident investigation can elucidate the potential causes and mechanisms of the collapse accident, thus remediating future structural collapse and enhancing the resilience. However, there are some obstacles to investigating complicated collapse accidents using conventional methods. For example, the out-syncs between on-site investigation and simulation analysis are intractable and can make discovering the cause of collapse accidents difficult. Hence, a digital twin-based investigation method for collapse accidents was proposed. First, basic virtual digital building models are established using real-world information. Then, after mapping the data from the real world into the virtual space, the corresponding highly realistic multistage models before and after the building collapse accident are constructed and synchronized. Using the digital twin method, investigators with multidisciplinary knowledge can efficiently integrate, update, and check the models. Finally, the potential collapse mechanism was revealed with the assistance of the corresponding models. To demonstrate the effectiveness of the proposed digital twin-based investigation method, a real collapse accident investigation is utilized as an example. These results validated our method.

1. Introduction

Safety during the service life is one of the most critical building requirements. However, in the last few decades, building collapse accidents have repeatedly occurred worldwide, causing severe injury, death, adverse social impact, and economic loss [1–4]. These catastrophic events have raised increasing concerns for engineers and researchers. To ensure integrity and safety, it is essential to analyze the potential causes of collapse, which will, in turn, provide valuable references for building design, construction, and maintenance, as well as collapse-prevention strategies.

Building collapse can be caused by several factors, making it difficult to identify the major causes [5–8]. Widely used building collapse investigation methods include (1) site-investigation methods [9, 10] and (2) simulation-based methods [4, 8]. Although widely used, these investigation methods are limited in more complex situations. Specifically, the site investigation method can hardly reproduce the collapse scenario of a building. The motion of fragments

determines the distribution of the debris, which is crucial for accident investigation [11]. As for simulation-based methods, the result of collapse analysis relies on quantifying uncertainties in building modeling [12]. An effective method for reducing the modeling uncertainties is updating the design document-based FE model with real-time measurement data [12]. However, the out-syncs between the on-site investigation and simulation-based analysis are intractable and can cause difficulties in determining the causation of collapse accidents. For the above reasons, new digital methods, combining site-investigation and numerical methods, need to be proposed to assist the investigation.

The digital twin concept originated from Grieves and Vickers product lifecycle management model in 2002 [13]. A digital twin is a set of virtual information constructs which fully describes a potential or actual physical entity from the micro atomic to macro geometrical level [13]. The foundations of a digital twin can be divided into four parts: (1) modeling and simulation of a physical entity to build the corresponding virtual entity and connections; (2) data

collection and data fusion for physical, virtual, and fusion data between them; (3) interaction and collaboration between the physical and virtual entities; and (4) relevant theories of service [14]. The digital twin is a fast-evolving technology, and many researchers have explored its application in the smart manufacturing [15, 16] and automated product-service systems [17]. Nowadays, the digital twin technology has expanded to the civil engineering sector [18]. Liu et al. [19] established a digital twin multidimensional model of prestressed steel structures for the safety risk assessment of prestressed steel structures. Peng et al. [20] reported a digital twin system of a hospital, by which the quality of daily maintenance work was enhanced. Lu and Brilakis [21] delivered a slicing-based object-fitting method that can generate the geometric digital twin of an existing reinforced concrete bridge from a labeled point cluster. Shim et al. [22] developed a bridge maintenance system for prestressed concrete bridges using a 3D digital twin model. Angjeliu et al. [23] studied the structural system integrity of historic masonry buildings by developing the concept of digital twins. The digital twin can also be used in retrofitting and demolishing because of its ability to comprehensively characterize the building to be renovated [24]. Previous studies have shown that, with the help of a digital twin, researchers can obtain a comprehensive understanding of the building and establish high-fidelity 3D models for simulation and mechanical calculation. Therefore, the digital twin has the potential to become an effective tool for analyzing the cause of building collapse.

In this study, a digital twin-based building collapse investigation method is proposed. Digital twin-based collapse analysis techniques have been proposed and used to simulate the entire life cycle of a building and then reproduce the building collapse accident. Specifically, building information models (BIM), finite element models (FEM), and physics engine models of the building were established to simulate the performance of the building during operation and maintenance. Subsequently, the main causes of building collapse were analyzed and expounded. The results indicate that defects and damage in critical regions of buildings are important factors that can cause building collapse. The rationality of the digital twin-based virtual model analysis was validated by site investigation. The results show that digital twin techniques are powerful tools for analyzing the cause of building collapse.

2. Digital Twin-Based Collapse Investigation Method

It is difficult to effectively determine the cause of building collapse using traditional analysis methods, such as on-site investigations and surveillance videos. Hence, this study proposed a digital twin-based collapse investigation method to elucidate the causes of building collapse. Figure 1 presents the conceptual architecture of the digital twin-based collapse investigation method, which considers the critical changes throughout the building life cycle (i.e., from construction to collapse). The digital twin model consists of two components: physical models (in the real

world) and virtual models (in digital space). The building information was continuously exchanged between the two models. Specifically, the interaction between the physical and virtual spaces involves three steps: Step 1: data collection and modeling, Step 2: construction and updating, and Step 3: on-site investigation and simulation. Furthermore, the workflow of the proposed digital twin-based method incorporating physical models, building information models (BIMs), and finite element models (FEMs) is briefly presented in the following:

> Step 1: data collection and modeling. First, necessary information, such as architectural, structural, and construction drawing details of the building, should be collected from the physical model. Then, the virtual models, including the BIMs and FEMs of the building, are established based on the collected information. In this stage, information flows from the physical model to the virtual model.

> Step 2: construction and updating. On the one hand, the virtual models are constantly updated as more building information is collected from the physical model. For example, when the construction and renovation information of a building is available, virtual models can simulate the renovation and construction process based on the information. On the other hand, some mechanisms may be revealed by simulating virtual models, which can better guide the information search process in the real world. In other words, the virtual model provided decision support to the physical world. For example, a column approaching instability can be identified via virtual model analysis, indicating that column failure is likely to cause building collapse. Therefore, more attention should be paid to the column of the building during the search process in the physical model. In this stage, information is iteratively exchanged between the physical and virtual models.

> Step 3: on-site investigation and simulation. After collecting sufficient data from the physical model, the virtual model is utilized to reproduce building collapse and reveal the underlying causes. Finally, the debris from the collapsed building simulated from the virtual model is compared with real debris, which validates the collapse mechanism determined from the virtual model analysis. In this stage, information flows from the virtual model to the physical model.

Moreover, a real building collapse accident was utilized to illustrate the proposed method. Accordingly, the details of Steps 1–3 are shown in Sections 3–5, respectively. Finally, Section 6 concludes the study.

3. Digital Twin of the Building

3.1. Collapse Accident of a Building. The adopted case is the collapse accident of a seven-story building (Figure 2(a)). The building collapsed after welding strengthening in 2020, and the debris is shown in Figure 2(b). The collapsed building was initially a conventional steel frame structure. However,
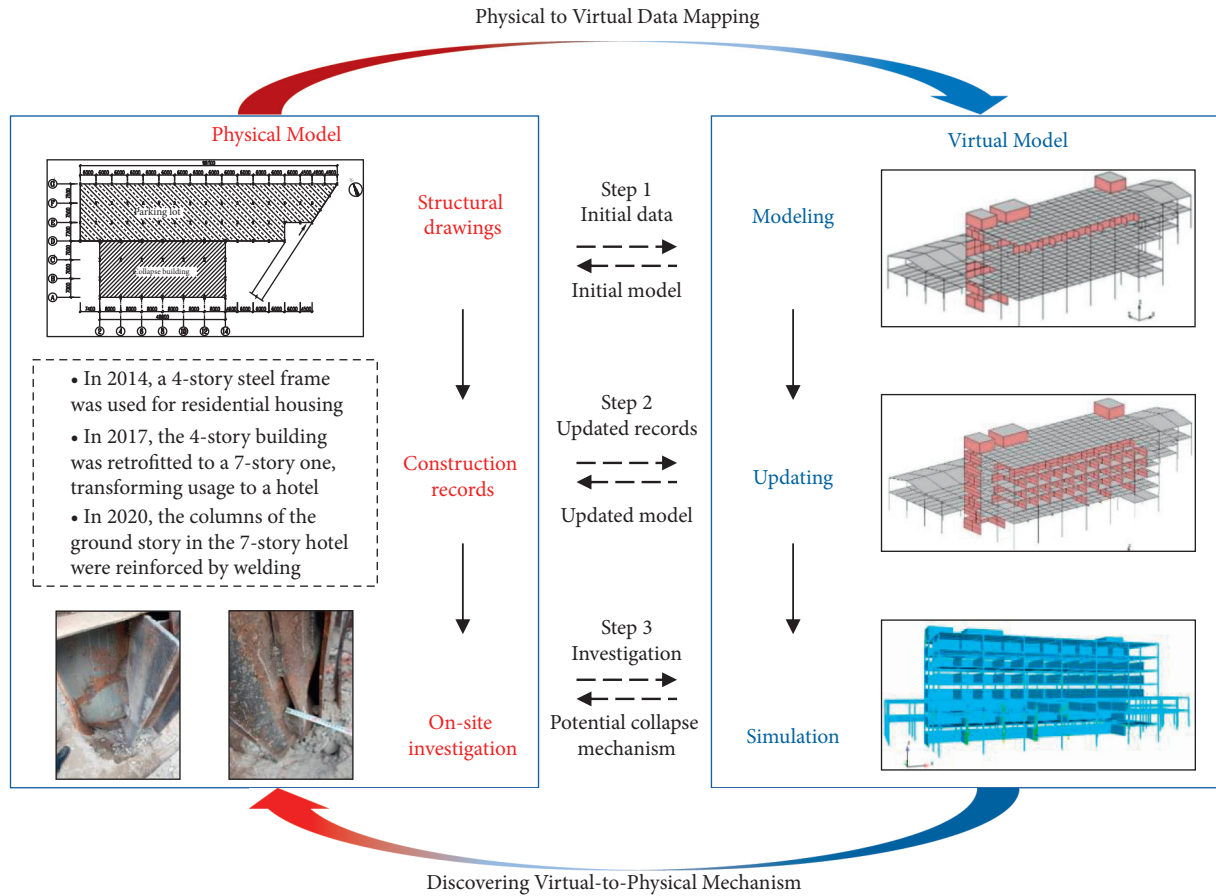
Physical to Virtual Data Mapping

FIGURE 1: Architecture of the proposed digital twin-based collapse investigation method.

the building underwent many functional changes over the years, and its structure changed correspondingly. Therefore, the complex retrofitting process and irregular internal structure led to complicated loading states and collapse accidents. The complex retrofitting process also makes it difficult to reveal the potential collapse mechanism using conventional analysis methods. The digital twin-based collapse investigation method can provide a comprehensive and accurate understanding of the building at each stage from construction to collapse. Therefore, to establish the digital twin model, we collected the necessary information about the building from construction to collapse. Based on this information, we established the corresponding digital twin models (see Section 3) and updated the models several times from the initial state to the critical state before collapse (see Section 4).

3.2. Building Information and Data Acquirement.
The building was retrofitted many times, and the major retrofitting processes are briefly presented in Figure 3. In the first stage, the building was a four-story commercial building, and the building was safe. In the second stage, the building underwent major retrofitting. Subsequently, the building was remodeled into a seven-story hotel. In the third stage, welding strengthening was applied to the base columns of the building. Subsequently, the building collapsed.

The plane view and elevation view of the building in Stage 2 are shown in Figure 4. The height of the collapsed building is 22 m. The length of the building in the east–west direction is 48 m, with 8 m × 6 spans, and the length of the building in the north–south direction is 21 m, with 7 m × 3 spans.

The building is a steel frame structure, and the primary components, that is, the column, beam, infill wall, and floor, should be created in the virtual models. The beams and columns were all equipped with H-shaped cross-sections, and their material strengths were determined according to the on-site test results. The yield strength F_y of the steel columns was 336 MPa, and the yield strength F_y of the steel beams was 313 MPa. The elastic modulus, E_s, of the steel beams and steel columns was 205 GPa. A detailed steel column layout drawing of the typical floors of the building is shown in Figure 5(a). A detailed steel beam layout drawing of the typical floors is shown in Figure 5(b). In terms of the infill walls, the strength grade of the bricks in the building infill wall was MU10. The standard value of compressive strength according to the *Code for Design of Masonry Structures* [25] is 1.48 MPa, and the elastic modulus is 1.165 GPa. The strength grade of the concrete in the slab is C20. The standard value of compressive strength according to the *Code for Design of Concrete Structure* [26] is 13.4 MPa, and the elastic modulus is 25.5 GPa. Furthermore, the on-site investigation revealed that the thickness of the structural floor used in the virtual models was 130 mm.

(a)   (b)

FIGURE 2: Hotel building before and after the collapse. (a) The hotel building before collapse (the hotel name is anonymous). (b) Ruin after the collapse.
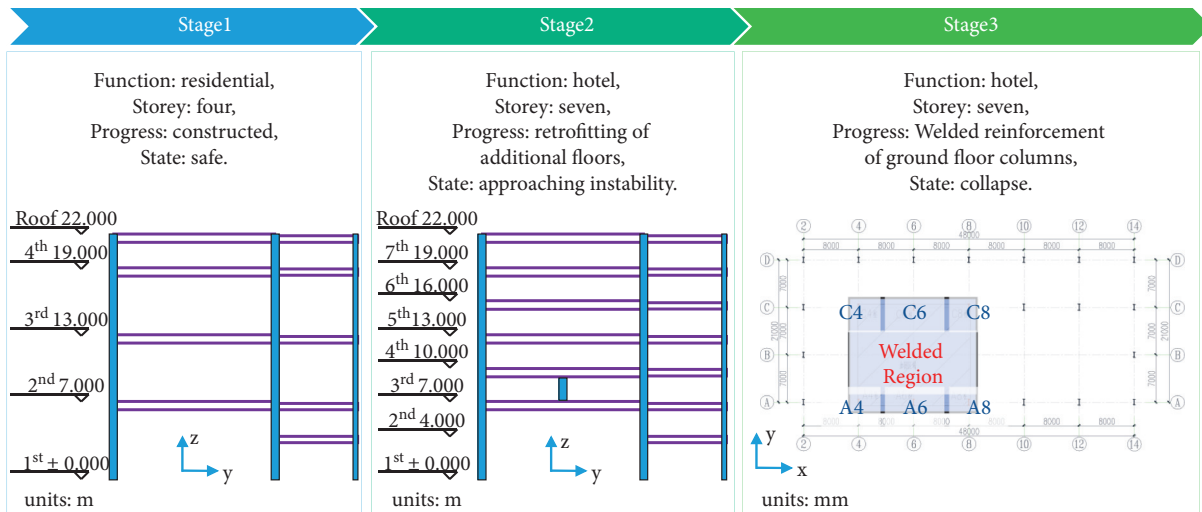
FIGURE 3: Conversion of the building.

(a)   (b)
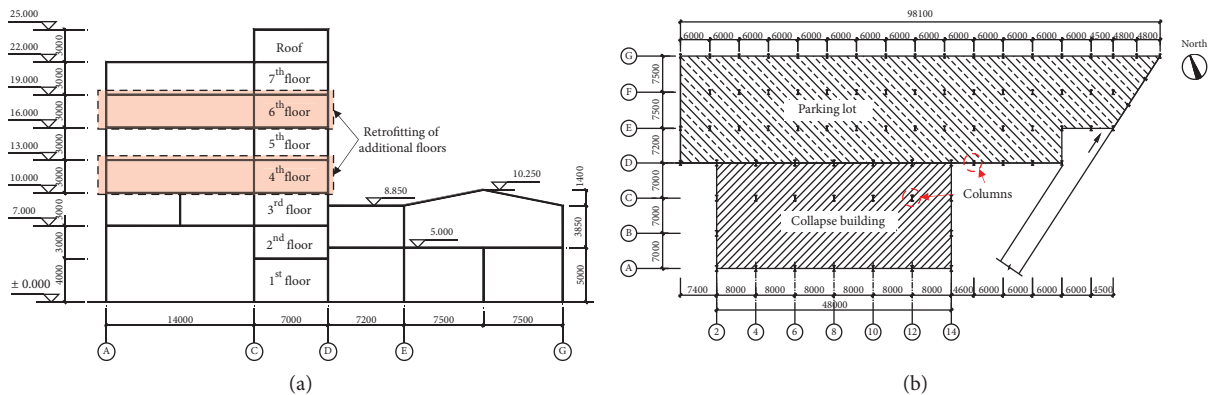
FIGURE 4: Basic views of the building. (a) Elevation view (the elevation units: m; other units: mm). (b) Plane view (units: mm).

After additional floors were retrofitted, the building transitioned from Stage 1 to Stage 2. The floors and infill walls were added to the structure, and the floor load was changed. In this study, the floor load values of the structure of all stages were calculated based on detailed structural information, including the decoration of floor slab and infill walls, self-weight of slabs, infill walls, ceilings, and glass curtain walls. The floor load values are listed in Table 1.

(a)

(b)

(c)
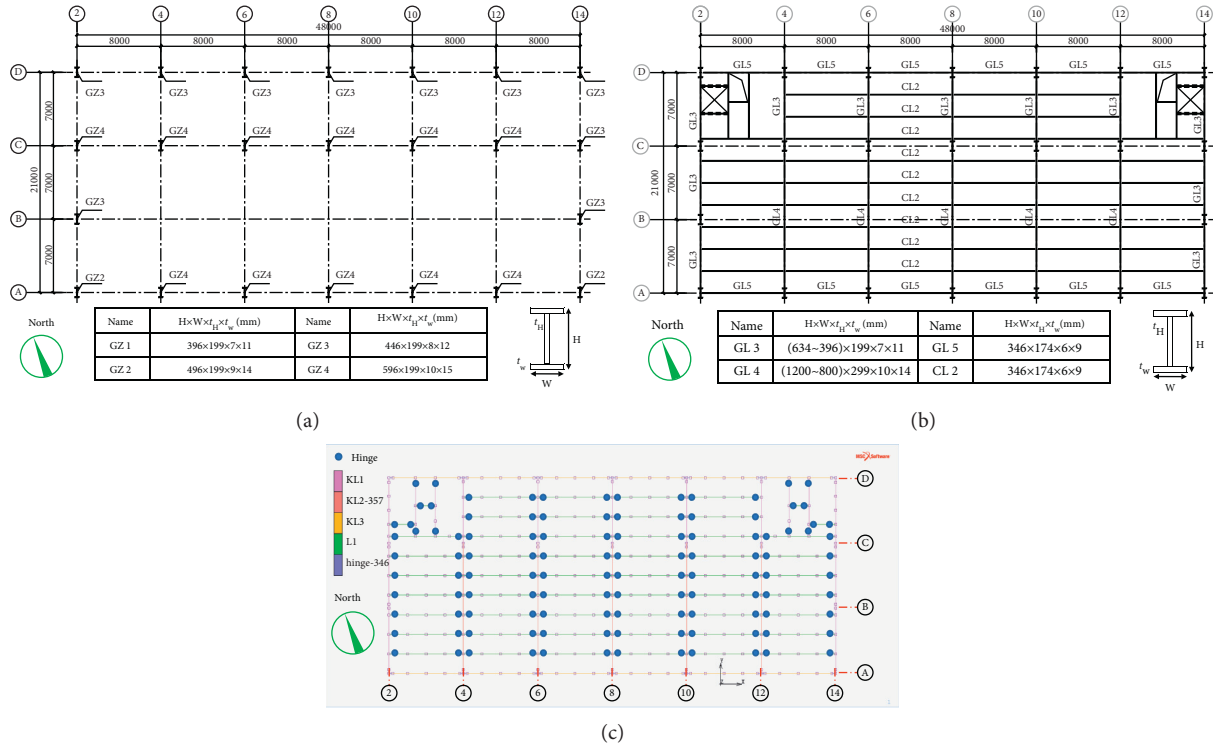
Figure 5: Drawings of the typical floor. (a) Column layout (units: mm). (b) Beam layout (units: mm). (c) Connections between beam and columns.

Table 1: Floor load of the building.

Floor number	Load of Stage 1		Floor number	Load of Stages 2 and 3	
	Dead load (kN/m^2)	Live load (kN/m^2)		Dead load (kN/m^2)	Live load (kN/m^2)
2nd	3.35	1.00	2nd	3.35	0.01
3rd	4.60	0.00	3rd	5.30	0.01
4th	4.30	0.00	4th	4.05	0.05
5th	5.30	1.00	5th	4.80	0.05
Roof	4.10	0.00	6th	4.43	0.05
			7th	4.80	0.02
			Roof	4.10	0.00

*Note that we collected detailed structural component dimensions, structural layout drawings, and material information from the building. Owing to copyright, only the most relevant information is presented in this paper.

3.3. Digital Twin Model Development.

After collecting the data from the physical model, the BIM of the building in Stage 1 was established using Revit [27] for effective data integration, as shown in Figure 6. BIM can effectively integrate the relevant information and data (e.g., the location of the infill walls, detailed cross section of beams and columns, and material information) from the physical model. Therefore, BIM is the basis of subsequent FEMs and physics engine models.

Subsequently, based on the detailed information provided by the BIM, a 3D FEM of the overall structure in Stage 1 was established using MSC.MARC [28]. Various types of elements are used to simulate different building components, considering their compatibility. The beams and columns were modeled with fiber beam elements considering the local buckling effect [29]. The infill brick walls were modeled using shell elements. The slabs were modeled using membrane elements. The adopted modeling methods have been widely used in previous studies [29–31]. The cross-sectional dimensions and structural layout are shown in Figures 4 and 5, respectively. The beams along the A-axis direction were primarily hinged and connected to the corresponding columns. Therefore, the rbe2 element [28] was used to model the hinged connection, releasing the rotational degree-of-freedom. Meanwhile, the beams along the 2-axis are rigidly connected to the corresponding columns. The typical connections between the beams and columns are shown in Figure 5(c). The steel columns of the base floor were rigidly connected to the ground. The above-mentioned building modifications are illustrated in Section 4.

4. Digital Twin Model Updating

4.1. Model Updating of BIM Based on Construction Log. From the information collected from the construction logs, the key processes for the major retrofitting of additional stories are as follows:

Step 1: steel column construction on the third floor (7–10 m)

Step 2: steel beams and floor slab construction of the fourth floor (10 m); interior wall construction on the third floor

Step 3: interior wall construction on the fourth floor

Step 4: interior wall construction on the fifth floor

Step 5: reinforced concrete floor slab construction on the sixth floor (16 m)

Step 6: interior wall construction on the sixth floor

Step 7: elevator installation and elevator machine room construction on the roof

Step 8: window and door installation, and water tank installation on the roof

Step 9: covering the steel columns of the first floor with 800×800 mm wooden boards and covering the steel columns on the D-axis with ceramic tiles

The BIM is then updated based on construction log information. The BIM before the update (i.e., Stage 1) is shown in Figure 7(a), and the updated BIM is shown in Figure 7(b). An animation of the construction process was created to demonstrate the major retrofitting of additional stories. Specifically, the Revit model is first exported as a Filmbox (FBX) file [32], and the FBX file is then imported into Twinmotion [33]. The construction process is then simulated. Continuous screenshots of the construction process are presented in Figure 8.

The intuitive and visual nature of BIM also provided a useful aid to understanding the layout and retrofitting process. The powerful visualization display ensures smooth communication and close cooperation among the multidisciplinary professionals on the investigation team. The digital twin-based method can better quantify the uncertainty of the virtual models. There are lots of uncertainties in the modeling process. If only simulation-based methods are used, the result of collapse analysis relies fully on quantifying uncertainties in building modeling [12]. If there was a discrepancy, the simulation result and the real world could be quite different. Thus, via utilizing the digital twin-based method, the BIM model of the digital twin model enables the domain experts in the physical world to carefully confirm and correct the virtual model to quantify and then reduce the uncertainties. An accurate digital model can provide critical support for the determination of structural loads and construction methods. This assists research and analysis to determine the causal factors of accidents.

4.2. Finite Element Model Updating and Analysis. Depending on the changes in the building structure and load determined by the BIM, the FEM is updated. The modeling method for FEMs based on MSC.MARC [28] is described in Section 3.2. To investigate the real-world state of the building, the actual loads are applied (i.e., 1.0 dead load + 1.0 live load). In addition, the pushdown method [31, 34, 35] was used to evaluate the vertical load safety redundancy of the structure in each phase. In the FEM, the pushdown method can be utilized by increasing the vertical load (i.e., simultaneously increasing the dead load and live load) until the structure collapses. The vertical load safety redundancy was obtained by dividing the collapse load by the current vertical load:

(1) *Stage 1.* The initial structure before retrofitting is four stories. The analysis results show that the total gravity load of the model before retrofitting was 3114 tons. The vertical ultimate bearing capacity of the structure calculated by finite element analysis was 5208 tons. Therefore, the total weight accounts for approximately 60% of the vertical ultimate bearing capacity. The maximum axial force of the first-story column was approximately 232 tons (C4), which was 63% of its stable ultimate bearing capacity. Therefore, the structure was in an elastic state (Figure 9(a)).

(2) *Stage 2.* The structure after the major retrofit had seven stories. The analysis results showed that the total gravity load of the modified model was 5214 tons, and the vertical load increased by 67%. The analysis results showed that the vertical ultimate bearing capacity of the structure was 5312 tons. Therefore, the total weight accounts for approximately 98% of the vertical ultimate bearing capacity and exceeds the vertical ultimate bearing capacity of the original four-story structure of 5208 tons. The maximum axial force of the first-story column is approximately 389 tons (C8), which is 105% of the theoretical ultimate load-carrying capacity of the column on the C-axis. The maximum compressive stresses in the web plates of steel columns C6, C8, and C10 in the structure exceeded their buckling stress. The structure was in a critical state (Figure 9(b)).

(3) *Stage 3.* After the welding strengthening in Stage 3, the building collapsed. According to the analysis results of the FEM of Stage 2, the total structural gravity load of the retrofitted 7-story steel structure under the actual use load is 5214 tons, which is very close to the vertical ultimate bearing capacity (Figure 9(c)). Although the bottom columns were in a critical state and plastic deformation occurred, the structure did not collapse. This suggests that the immediate cause of building collapse requires further investigation.

According to the BIM construction process, the structure collapsed after welding strengthening on the partial columns on the ground story. Therefore, the results of the analysis of the digital twin model indicate that the effects of welding need to be considered. The research team then conducted an on-site investigation. According to the on-site investigation results, in this welding construction, the lower
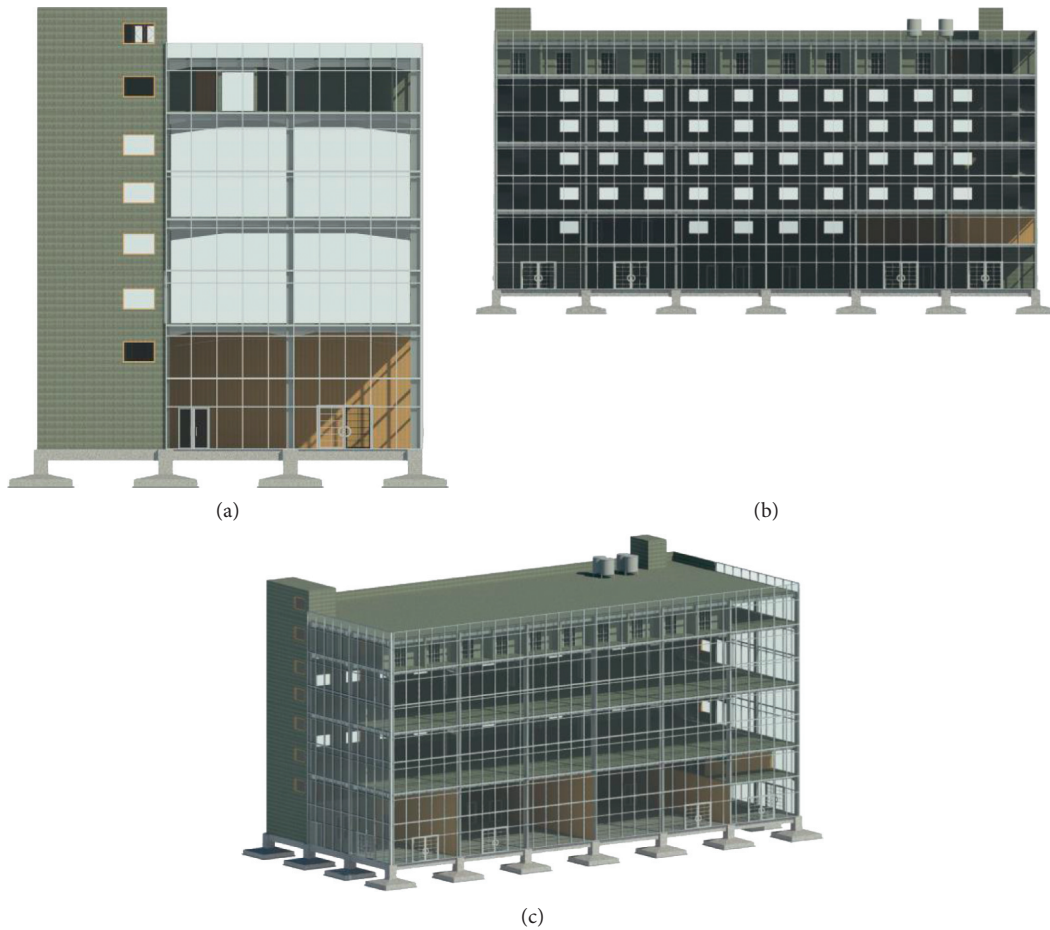
(a)

(b)

(c)

FIGURE 6: BIM of the building in Stage 1. (a) Left side view. (b) Front view. (c) Axonometric view.

More infill walls are added after retrofit

More floors are added after retrofit

(a)

(b)
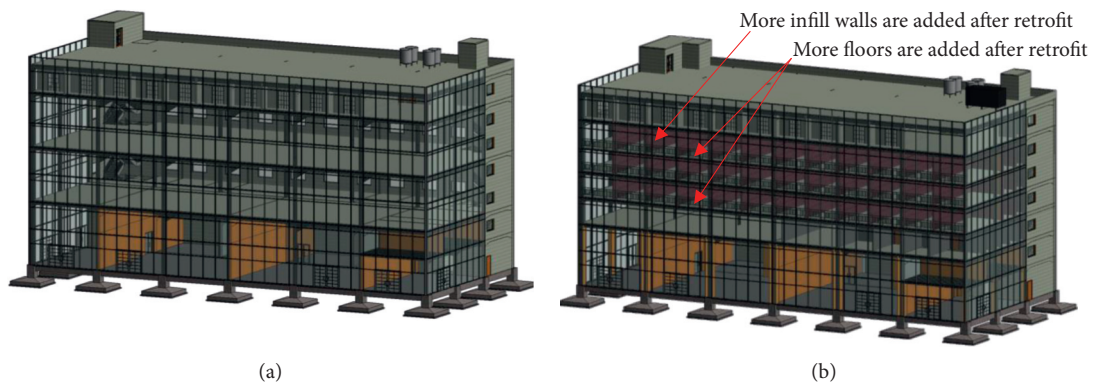
FIGURE 7: Updating the BIM. (a) Original model. (b) Updated model.

section of the steel columns (e.g., C4, C6, and C8) at the bottom introduced a horizontal deformation with an amplitude of 2–6 mm (Figure 9(d)). Thus, according to the on-site investigation results, the corresponding horizontal deformation was added to the FEM based on the analysis of Stage 2. Subsequently, the structure underwent initial collapse.

5. Collapse Analysis Using the Digital Twin Model

5.1. Analysis of the Collapse Mechanism. According to the on-site investigation results, horizontal deformation of 2–6 mm occurred at Stage 3. In the subsequent simulation, the structural plastic deformation and damage rapidly and
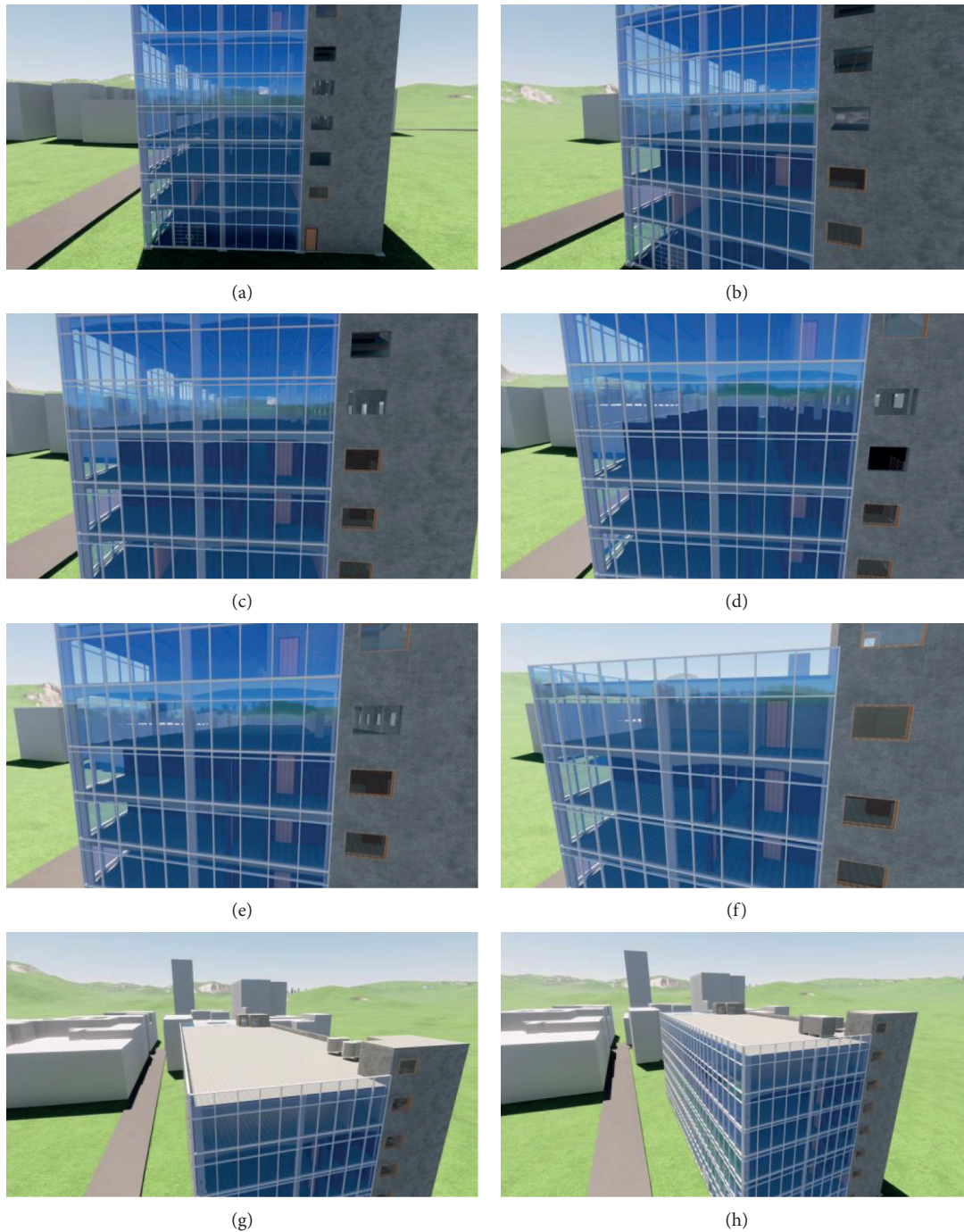
FIGURE 8: Updating the BIM animation. (a–h) Steps 1–8.

disproportionately propagated, and the structure entered the collapsed state, as shown in Figure 10.

Therefore, according to the finite element analysis results, the local buckling, plastic deformation, and flexural deformation of the bottom columns are increased by the welding construction. Taking the bottom C4 steel column as an example, the horizontal deformation in the middle increases by 2–4 mm. As a result, severe disturbances were generated owing to the high load, inducing damage to the

bottom steel columns and the overall collapse of the structure. Thus, the mechanism and critical causes of the structural collapse accident were determined.

5.2. Visualization of the Collapse Progress. To validate the building collapse mechanism via the virtual model analysis, a collapse visualization analysis was conducted using the collapse simulation technique based on the physics engine

(a)

(b)

(c)

(d)

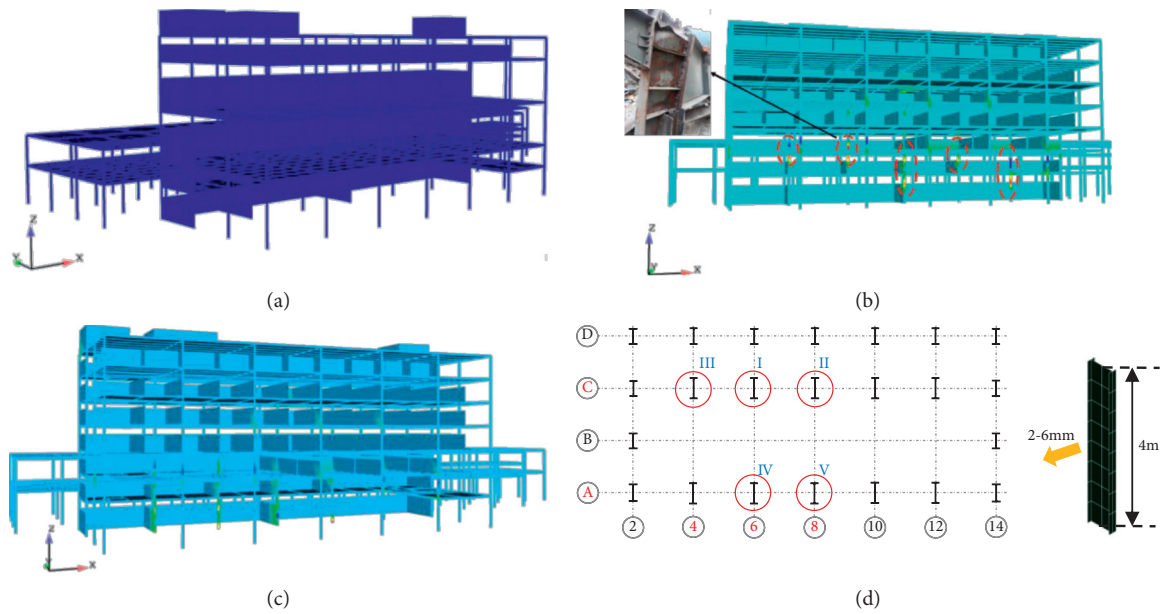Figure 9: Axial forces of the beams and columns of the building. (a) Stage 1. (b) Stage 2. (c) Stage 3. (d) Critical elements. (a) Stage 1: no damage. (b) Stage 2: plastic hinge at top of first story center column. (c) Stage 3: initial collapse. (d) Key columns causing structural collapse.
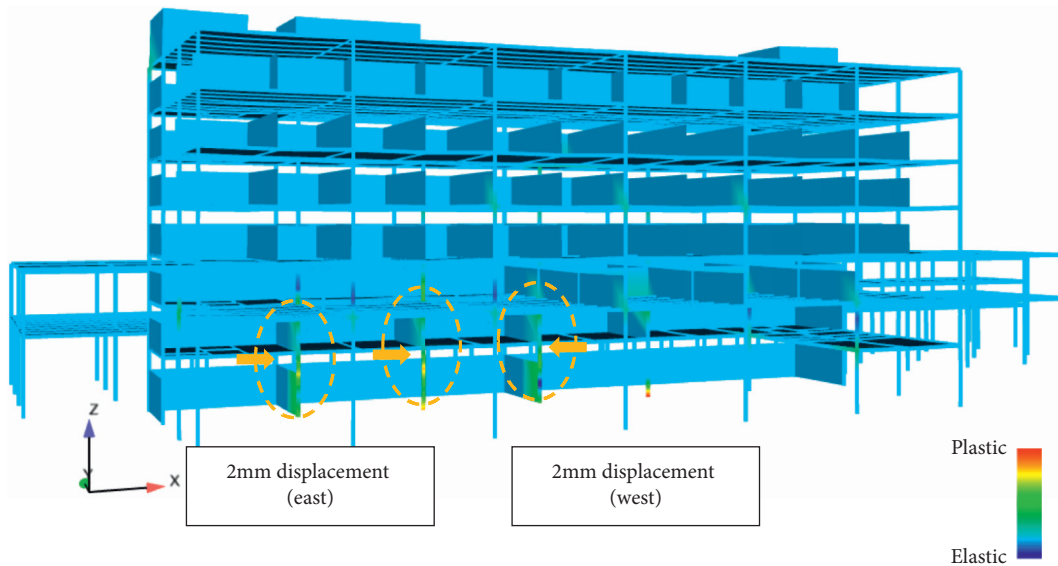

Figure 10: Collapse initial state of the building.

[4, 36, 37]. Subsequently, the simulated virtual wreckages were compared with the actual physical collapse wreckages at the site. The collapse visualization method proposed by Lu et al. [4] was adopted. The simulation is implemented in three primary steps: (1) geometric model establishment and conversion, (2) establishment of physics engine model, and (3) introduction of initial damage [4]. First, the FEM in the virtual model of the digital twin was utilized as the geometric model. Then, the geometric model was converted into a physics engine model using tools developed by Zheng et al. [36]. Subsequently, the initial disturbances are applied to the C4, C6, and C8 columns welded at the bottom of the physics engine model based on the causes of collapse identified in

Section 5.1. Finally, the collapse processes were simulated using the physics engine model, and the simulated collapse processes of the building are shown in Figure 11.

Initially, the middle steel column of the first floor on the A-axis bends in the east–west direction (Figure 11(b)). The vertical compressive bearing capacity of the steel column decreased rapidly, resulting in the steel column being unable to support the gravity weight of the upper structure. Subsequently, the upper structures, especially the parts of the three stories above the range from axis A to axis C, start to collapse. Meanwhile, the buildings started to tilt in the southern direction (Figure 11(c)). The span of the building along the C-axis to D-axis direction is 7 m, which is shorter
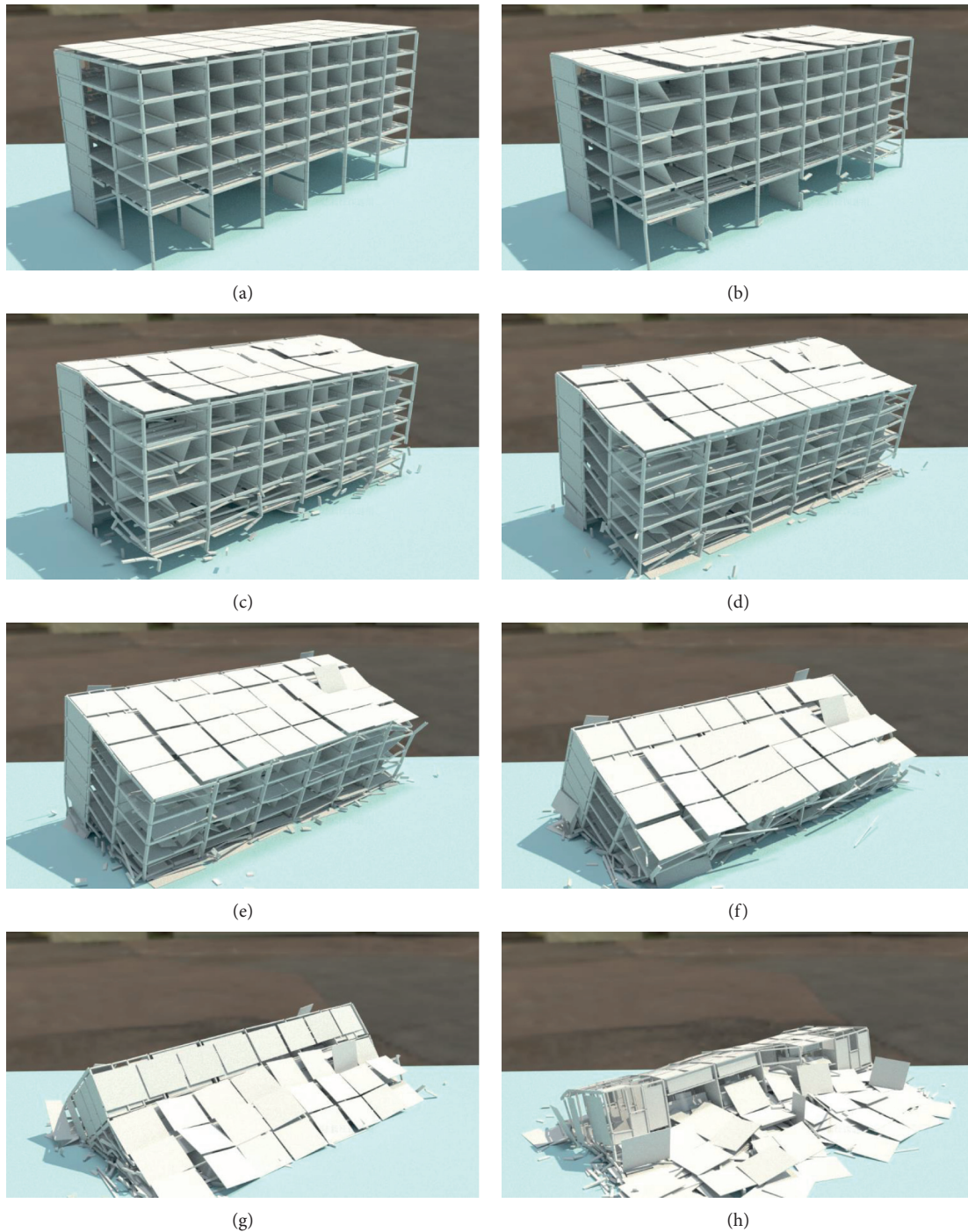
FIGURE 11: Collapse progress of the building. (a) Collapse begins; (b) column at A-axis starts buckling; (c) the columns on the first floor at the A-axis lose their vertical bearing capacity; (d) the third-floor slab at A-axis first touches the ground, and the upper structure tilts to the south; (e) the fourth-floor slab first touches the ground, and the upper structure severely tilts; (f) column at D-axis pulls off, and several floors at A-axis touch the ground; (g) the building tilts to the south and several upper floors touch the ground; (h) collapse process is complete.

than the span along the A-axis to the C-axis direction of 14 m. Moreover, there are more infill walls in the north–south direction along the C-axis to the D-axis than along the A-axis to the C-axis. The column at the A-axis gradually loses its load-carrying capacity, and the load from the upper structure is then transferred to the columns at the C-axis and D-axis.

This resulted in severe buckling of the column at the C-axis and accelerated the overall collapse of the upper structure. Subsequently, the third-floor slab near the A-axis first touched the ground (Figure 11(d)). Gradually, as the overall southward tilt deformation increased, the upper floors successively came to the ground. The column at the D-axis was

(a)

(b)

(c)

(d)

(e)

(f)

FIGURE 12: Comparison between actual physical collapse wreckages and simulated virtual wreckages. (a) Actual collapse scenario (side view); (b) simulated collapse scenario (side view); (c) actual collapse scenario (front view); (d) simulated collapse scenario (front view); (e) actual collapse scenario (top view); (f) simulated collapse scenario (top view).

subjected to increasing tension, and the bottom of the column was pulled off (Figure 11(f)). After that, the whole building fell toward the south, and the floor slab broke apart. Finally, the collapse process was completed, and only debris was left.

The simulated debris distribution of the building is shown in Figure 12; on the left are stills from the photos taken from the building site, and the right subfigures are the simulated results. Figure 12 shows that the simulated debris distribution agrees well with the actual collapse wreckage, indicating that the proposed collapse investigation method realistically reproduces the building collapse process.

5.3. Interaction in Virtual and Real Spaces to Reveal the Accident Mechanism. The above analysis validates the effectiveness of the proposed digital twin-based collapse analysis method. The method can reproduce the collapse process in the virtual space and, thus, assist in investigating the causes of collapse accidents. In addition, the proposed digital twin-based collapse analysis method also reveals that defects and damage in the critical areas of buildings are important factors causing building collapse, which implies that the critical regions should be identified as soon as possible. In practice, proper strengthening and monitoring

of these critical regions can effectively prevent building collapse.

Digital twin-based methods can better assist decision-making in the physical world. Collapse accident sites are dilapidated and chaotic, making it difficult to determine the cause of the collapse only using site investigation-based methods. On the one hand, the site investigation found local buckling of the ground floor columns. Therefore, the traditional methods may regard the local buckling as the cause of the collapse. However, the digital twin-based method pointed out that the local buckling was caused by the gravity load in Stage 2, which helps the investigation avoid being misled by the local buckling on-site and supports making a reasonable decision. On the other hand, the digital twin-based method pointed out that welding was the direct cause of the building collapse. The welding leads to an increase in the internal force of the component, which in turn causes the overall horizontal deformation of the component and then eventually leads to the collapse of the whole structure. The simulation results of the collapse mode are consistent with what happened in the physical world, which provides effective support for the accident investigation.

The analysis results in this work also provide practical strategies for future disaster prevention and control, such as strict investigation of structural retrofits, increasing the structural health monitoring technology, and developing a digital twin for disaster evolution.

6. Conclusions

Collapse accident sites are dilapidated and chaotic, making it difficult to determine the cause of collapse using traditional methods. Therefore, to improve the accident investigation, a digital twin-based accident investigation framework is proposed to conduct the investigation. The digital twin-based framework consists of the physical objects (e.g., structural drawings, construction records, and site investigation), the virtual model (e.g., BIM model, FE model, and physics engine model), and the interaction between the physical and virtual spaces. A real collapse accident and corresponding on-site investigation results were used to validate the proposed method. The results indicate that the digital twin-based method supports the decision-making process and the determination of real causes. Via the information interaction between the physical world and the virtual world, the real cause of the accident can be revealed more reliably. The major findings are summarized as follows:

(1) In the building collapse case, the maximum compressive stress in the columns on the ground floor of the building exceeded its critical buckling stress. The welding construction process led to local buckling and plastic deformation of the ground floor columns, which further resulted in large flexural deformation in the columns. This caused severe disturbance to the highly loaded steel columns, which induced damage to the columns on the ground floor and the overall collapse of the structure.

(2) With improvements in FEM, BIM, physics engine, and model updating techniques, the digital twin technology can be used for the collapse scenario simulation and cause investigation of structural collapse accidents. Even if the service history of the engineering structure is complex, the digital twin model can effectively record and update the series of changes, which can assist in the analysis of complex collapse mechanisms.

(3) The case study also demonstrates that the digital twin model has great potential for engineering disaster prevention and control. The digital twin model can provide effective data and platform support for performance evaluation and health monitoring of the structure.

This work is a preliminary exploration of digital twin-based accident investigations. The decision-making process is supported by digital twins, which helps to find the actual cause of the collapse accident. But the accident has already occurred and caused heavy losses. In future research, digital twin-based models are encouraged to be established for important buildings in advance to perform multihazard simulation analysis. In this way, the mechanical state of the key components of the building can be monitored all the time, thereby avoiding disasters.

Data Availability

All data requests and inquiries regarding this content should be directed to the corresponding author.

Conflicts of Interest

The authors declare no conflicts of interest.

Acknowledgments

References

[1] J. M. Adam, F. Parisi, J. Sagaseta, and X. Lu, "Research and practice on progressive collapse and robustness of building structures in the 21st century," *Engineering Structures*, vol. 173, pp. 122–149, 2018.

[2] H. Y. Luo, L. M. Zhang, H. J. Wang, and J. He, "Process of building collapse caused by the Po Shan Road landslide in Hong Kong on 18 June 1972," *Landslides*, vol. 18, no. 12, pp. 3769–3780, 2021.

[3] A. O. Windapo and J. O. Rotimi, "Contemporary issues in building collapse and its implications for sustainable development," *Buildings*, vol. 2, no. 3, pp. 283–299, 2012.

[4] X. Z. Lu, H. Guan, H. Sun et al., "A preliminary analysis and discussion of the condominium building collapse in surfside,

Florida, US, June 24, 2021," *Frontiers of Structural and Civil Engineering*, vol. 15, no. 5, pp. 1097–1110, 2021.

[5] W. Jing, S. Xing, and Y. Song, "Collapse-pounding dynamic responses of adjacent frame structures under earthquake action," *Advances in Civil Engineering*, vol. 2020, Article ID 8851307, 12 pages, 2020.

[6] S. Gao and S. Wang, "Progressive collapse analysis of latticed telecommunication towers under wind loads," *Advances in Civil Engineering*, vol. 2018, Article ID 3293506, 13 pages, 2018.

[7] S. A. Oloyede, C. B. Omoogun, and O. A. Akinjare, "Tackling causes of frequent building collapse in Nigeria," *Journal of Sustainable Development*, vol. 3, no. 3, p. 127, 2010.

[8] M. Tüfekci, E. Tüfekci, and A. Dikicioğlu, "Numerical investigation of the collapse of a steel truss roof and a probable reason of failure," *Applied Sciences*, vol. 10, no. 21, Article ID 7769, 2020.

[9] S. A. Oke, A. N. Amadi, A. E. Abalaka, and R. T. Akerele, "Results of subsoil investigation on a collapsed building site in Lagos, Nigeria," *Nigerian Journal of Construction Technology and Management*, vol. 10, no. 1&2, pp. 36–45, 2009.

[10] G. U. Alaneme, G. C. Ezeokpube, and E. M. Mbadike, "Failure analysis of a partially-collapsed building using analytical hierarchical process," *Reliability Engineering and Resilience*, vol. 2, no. 1, pp. 1–20, 2020.

[11] Z. Xu, X. Lu, H. Guan, and A. Ren, "Physics engine-driven visualization of deactivated elements and its application in bridge collapse simulation," *Automation in Construction*, vol. 35, pp. 471–481, 2013.

[12] K. Lin, Y.-L. Xu, X. Lu, Z. Guan, and J. Li, "Digital twin-based collapse fragility assessment of a long-span cable-stayed bridge under strong earthquakes," *Automation in Construction*, vol. 123, Article ID 103547, 2021.

[13] M. Grieves and J. Vickers, "Digital twin: mitigating unpredictable, undesirable emergent behavior in complex systems," in *Transdisciplinary Perspectives on Complex Systems*, FJ. Kahlen, S. Flumerfelt, and A. Alves, Eds., Springer, Cham, pp. 85–113, 2017.

[14] F. Tao, H. Zhang, A. Liu, and A. Y. Nee, "Digital twin in industry: state-of-the-art," *IEEE Transactions on Industrial Informatics*, vol. 15, no. 4, pp. 2405–2415, 2018.

[15] J. Leng, M. Zhou, Y. Xiao et al., "Digital twins-based remote semi-physical commissioning of flow-type smart manufacturing systems," *Journal of Cleaner Production*, vol. 306, Article ID 127278, 2021.

[16] Q. Liu, J. Leng, D. Yan et al., "Digital twin-based designing of the configuration, motion, control, and optimization model of a flow-type smart manufacturing system," *Journal of Manufacturing Systems*, vol. 58, pp. 52–64, 2021.

[17] J. Leng, D. Yan, Q. Liu et al., "Digital twin-driven joint optimisation of packing and storage assignment in large-scale automated high-rise warehouse product-service system," *International Journal of Computer Integrated Manufacturing*, vol. 34, no. 7-8, pp. 783–800, 2021.

[18] F. Jiang, L. Ma, T. Broyd, and K. Chen, "Digital twin and its implementations in the civil engineering sector," *Automation in Construction*, vol. 130, Article ID 103838, 2021.

[19] Z. Liu, W. Bai, X. Du, A. Zhang, Z. Xing, and A. Jiang, "Digital twin-based safety evaluation of prestressed steel structure," *Advances in Civil Engineering*, vol. 2020, Article ID 8888876, 10 pages, 2020.

[20] Y. Peng, M. Zhang, F. Yu, J. Xu, and S. Gao, "Digital twin hospital buildings: an exemplary case study through continuous lifecycle integration," *Advances in Civil Engineering*, vol. 2020, Article ID 8846667, 13 pages, 2020.

[21] R. Lu and I. Brilakis, "Digital twinning of existing reinforced concrete bridges from labelled point clusters," *Automation in Construction*, vol. 105, Article ID 102837, 2019.

[22] C.-S. Shim, N.-S. Dang, S. Lon, and C.-H. Jeon, "Development of a bridge maintenance system for prestressed concrete bridges using 3D digital twin model," *Structure and Infrastructure Engineering*, vol. 15, no. 10, pp. 1319–1332, 2019.

[23] G. Angjeliu, D. Coronelli, and G. Cardani, "Development of the simulation model for Digital Twin applications in historical masonry buildings: the integration between numerical and experimental reality," *Computers & Structures*, vol. 238, Article ID 106282, 2020.

[24] Ö. Göçer, Y. Hua, and K. Göçer, "A BIM-GIS integrated pre-retrofit model for building data mapping," *Building Simulation*, vol. 9, no. 5, pp. 513–527, 2016.

[25] GB 50003-2011, *Code for Design of Masonry Structures*, National Standards of People's Republic of China, China, 2011.

[26] GB 50010-2010, *Code for Design of concrete Structures*, National Standards of People's Republic of China, China, 2015.

[27] L. Khemlani, *Autodesk Revit: Implementation in Practice*, White paper, Autodesk, CA, 2004.

[28] MSC, *Marc, Volume A: Theory and User Information*, MSC. Software Corporation, Newport Beach, CA, 2012.

[29] X. Z. Lu, C. Zhang, W. Liao, Y. Lin, X. Lin, and H. Xue, "Comparison of seismic performance between typical structural steel buildings designed following the Chinese and United States codes," *Advances in Structural Engineering*, vol. 24, no. 9, pp. 1828–1846, 2021.

[30] Y. Bai and X. Lin, "Numerical simulation on seismic collapse of thin-walled steel moment frames considering post local buckling behavior," *Thin-Walled Structures*, vol. 94, pp. 424–434, 2015.

[31] K. Lin, Y. Li, X. Lu, and H. Guan, "Effects of seismic and progressive collapse designs on the vulnerability of RC frame structures," *Journal of Performance of Constructed Facilities*, vol. 31, no. 1, Article ID 04016079, 2017.

[32] A. Autodesk (2021). FBX SDK documentation. Available at: https://docs.autodesk.com/FBX/2014/ENU/FBX-SDK-Documentation/index.html.

[33] Twinmotion (2021). Twinmotion. Available at: https://www.twinmotion.com/en-US.

[34] C. T. Fallon, S. E. Quiel, and C. J. Naito, "Uniform pushdown approach for quantifying building-frame robustness and the consequence of disproportionate collapse," *Journal of Performance of Constructed Facilities*, vol. 30, no. 6, Article ID 04016060, 2016.

[35] M.-H. Tsai and W.-B. Zhuang, "An analytical approach for the flexural robustness of seismically designed RC building frames against progressive collapse," *International Journal of Civil Engineering*, vol. 18, no. 9, pp. 1025–1037, 2020.

[36] Z. Zheng, Y. Tian, Z. Yang, and X. Lu, "Hybrid framework for simulating building collapse and ruin scenarios using finite element method and physics engine," *Applied Sciences*, vol. 10, no. 12, Article ID 4408, 2020.

[37] W. Oliver and K. Kostack, "Final release of the Blender and Bullet physics engine based on fast on-site assessment tool," 2017, https://inachuslaurea.files.wordpress.com/2019/07/inachus_d3.5_luas_v1.0.pdf.